Article type: Full Paper

Highly flexible, large-area and facile textile-based hybrid nanogenerator with cascaded piezoelectric and triboelectric units for mechanical energy harvesting

*Jian Song, Bao Yang, Wei Zeng, Zehua Peng, Shuping Liu, Jun Li, Xiaoming Tao**

Nanotechnology Center of Functional and Intelligent Textiles and Apparel, Institute of Textiles and Clothing, The Hong Kong Polytechnic University, Hong Kong, China.

E-mail: xiao-ming. tao@polyu.edu.hk

Keywords: flexible, large-scale, hybrid nanogenerator, theoretical analysis, mechanical energy harvesting

Abstract:

Despite of the rapid development and demonstrations of wearable energy harvesting devices, their industrial applications have been limited by the lack of highly flexible, scalable and facile fabrication method. Especially, few studies have involved the theoretical analysis with the relevant experimental verification. To this end, we demonstrate a highly flexible and large-area textile-based hybrid nanogenerator integrated a net-shaped nanofiber reinforced piezoelectric unit and a triboelectric unit with a micro-structured surface configuration. Electrospinning technique was used to fabricate an optimized PVDF-CNT-$BaTiO_3$ nanofiber/particle nonwoven fabric of 18 cm×27 cm for the piezoelectric unit without further polarization. Then a large-area free-standing PDMS-MWCNT-Graphite flexible composite film of 20 cm×25 cm, optimized for the triboelectric unit was prepared by doctor-blading method. The resultant hybrid nanogenerator, with 4.5 cm×5 cm in size, generated a rectified average peak output voltage of 161.66 V, along with the highest peak power output of 2.22 W/m^2, directly driving 150 LEDs. Importantly, explicit theoretical model for the hybrid nanogenerator were proposed and good agreements were obtained between the theoretical and corresponding experimental results, which sheds new lights on the mechanism and predicts the ways to optimize such hybrid nanogenerators.

1. Introduction

Energy crisis and environmental pollution have become a significant threat to the development of human society.[1] Likewise, the rapid growth of mobile, portable and wearable electronics devices are urgently in need of matching power pack. More importantly, future microelectronic systems have a great demand for harvesting energy from human movements or having self-powered devices.[2, 3] In the past decades, flexible energy harvesting devices driven by piezoelectric or triboelectric mechanisms have been extensively explored not only to deal with the global energy crisis, but also to realize the self-powered microelectronics integrated into clothing.[4, 5-7] Therefore, major research efforts have been recently made toward enhancing the electrical output of these nanogenerators via novel nanostructures or nanomaterials.[8, 9, 10]

In the piezoelectric aspect, various types of nanogenerators based on inorganic noncentrosymmetric materials, such as lead PZT,[11] ZnO[12, 13] and lead- free ceramics $BaTiO_3$,[14] as well as organic polymers, i.e. PVDF and PTFE, have been developed for energy harvesting applications. But, the intrinsic brittle and small strain characteristics in these inorganic materials also limits the further application in flexible electronic devices for such inorganic materials. Therefore, more and more piezoelectric devices have integrated the inorganic nanomaterials into flexible organic polymers. It has been reported that the polarized $BaTiO_3$/PVDF[15] and $BiFeO_3$/ PVDF[14] piezoelectric nanogenerators (PENG) not only have a high output performance, but also possess the flexible and transparent characteristics. In the triboelectric aspect, after the first report in 2012 by Wang and his co-workers,[16] the triboelectric nanogenerator (TENG) has been highlighted as an emerging system to meet a common need as an effective and sustainable energy source via converting random and irregular mechanical energy into usable electrical energy. The basic operation modes can be classified into four modes, namely vertical contact mode,[8, 17, 18] sliding mode and single-electrode mode and free-standing mode.[19] It has been reported that the output performance of TENG is much higher than that of electromagnetics and piezoelectrics,[13] giving rise to more attention for its applications in self-powered electronic device. Yet, since the occurrence of piezoelectric effect is usually accompanies by triboelectric effect, hybrid nanogenerators (HNG) with cascaded piezoelectric and triboelectric units have been recently examined in order to further enhance the output capacity of devices.[3, 6, 20] Such nanogenerators possess many advantages in the case of contact mode because of facile integration process and short vertical displacement.[8, 17] Tao and co-workers [8] theoretically investigated the operation mechanism of a contact-mode hybrid nanogenerator, and illustrated that the HNG can

effectively utilize the comprehensive piezoelectric and triboelectric effect to improve the overall output performance. Li et al.[6] developed a multilayered flexible hybrid nanogenerator by conjuction of piezoelectricity and triboelectricity, and results demonstrate that the polarization direction and doping content of $BiTiO_3$ are the two principal factors affecting the electrical output.

Although various types of nanogenerators have been proposed and further developed, there are still several issues to be overcome for the design and applications. First, how to fabricate highly flexible and large-scale energy harvesting nanogenerators by using facile methods to further develop the industrial scale production of such devices? Second, what kinds of hybrid nanogenerators with cascaded TENG and PENG have the best performance in the case of various contents of component materials and surface configurations? Last but not least, how to predict the output characteristics of a specified hybrid nanogenerator and working conditions?

To answer them, we will take up four challenging tasks in this study of flexible, large-scale and textile-based hybrid nanogenerator (T-HNG). First, we explored a novel hybrid nanogenerator with cascaded piezoelectric unit (PEU) and triboelectric unit (TEU). This hybrid nanogenerator cascades net-shaped PVDF nanofiber composite layer and carbon reinforced PDMS composite layer, which has highly flexible and large-area characteristics. Likewise, the electrospinning and doctor-blading techniques were used to fabricate this T-HNG, which saves a relatively complicated polarization process for piezoelectric unit, and free-standing PDMS composite film can be facile peel-off from the substrate. Second, to enhance the output performance of T-HNG, inexpensive sandpapers with different surface roughness were directly used as substrate to form the relatively uniform microstructure of PDMS composite film. Cost effective carbon materials, i.e. multi-wall carbon nanotube (MWCNT) and graphite, were introduced into the PEU and TEU. Third, fabrication, optimization and testing of T-HNG were conducted. In parallel, numeric simulation and theoretical modeling were carried out with corresponding experimental verification. We hope that the methods and findings will be helpful to design the highly flexible textile-based hybrid nanogenerators more facile, low-cost and suitable for industrial applications in the wearable device fields.

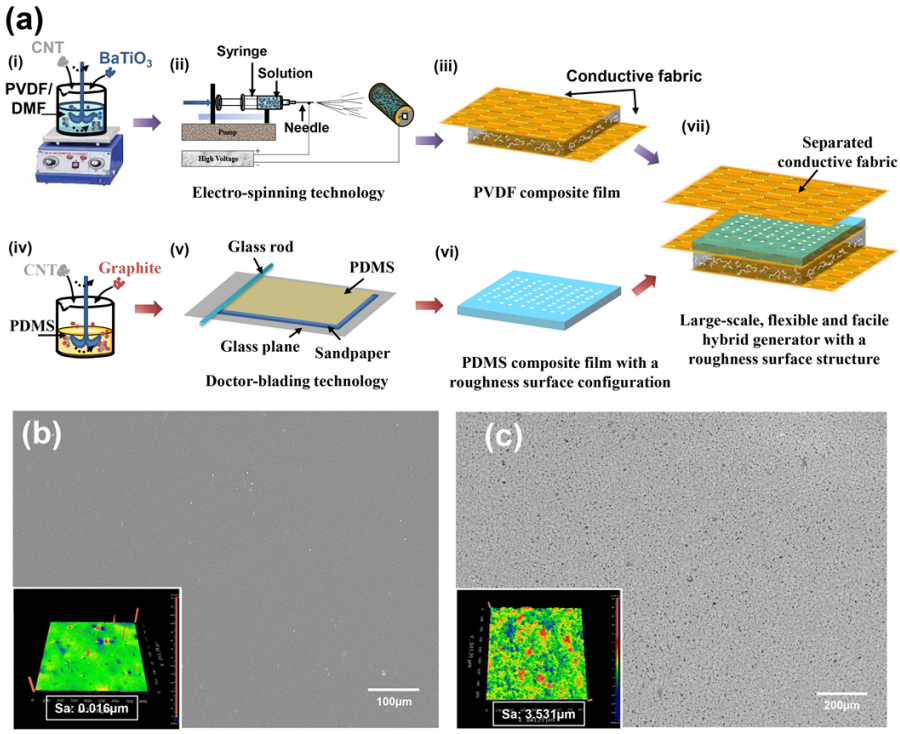

Figure 1. Schematic illustration of fabrication for the flexible, large-scale and facile hybrid nanogenerator with micro-pattern surface structure and surface morphology. (a) Facile fabrication flowchart for the piezoelectric and triboelectric units of T-HNG. (b) The top surface of PDMS composite film without micropattern structure; Inset displays the related measure result of surface roughness. (c) The bottom surface of PDMS composite film with amount of micropattern structure obtained by a P3000 sandpaper (P*: grit, European Standard). Inset exhibits the related measure result of surface roughness.

2. Results

Figure 1 exhibits the schmatic illustion of fabrication for the flexible and large-scale hybrid nanogenerator with micro-structure characteristic. The detail process was given in *Experiemntal Section*.

2.1. Characterization of hybrid generators

As observed in the schematic illustration in **Figure 2a**, the T-HNG consists of four layers, viz. three sets of fabric electrodes, PVDF/CNT/$BaTiO_3$ composite film as the piezoelectric unit and PDMS/CNT/Graphite composite film as the triboelectric unit, where the piezoelectricity and triboelectricity are aligned in a cascaded mode. Specifically, the top fabric electrode is separated with the other parts, which effectively provides a flexible and various approaches to design the triboelectric part. Figure 2b shows a digital photograph of T-HNG, demonstrating that the as-prepared T-HNG is flexible and can be even bent into a cambered surface. Figure 2c, d exhibit the as-prepared large-scale PVDF composite film (27 cm×18 cm) and PDMS composite film (25 cm×20 cm). To match with the sizes of both films, the dimension of conductive fabric is designed into 28 cm×19 cm shown in Figure 2e. The

initial T-HNG can be prepared by cascading the mentioned components, and subsequently it will be cut into small samples with a dimension of 4.5 cm×5 cm, which can be easily bent into 180° (Figure 2b). A cross-sectional scanning electron microscopy (SEM) image is displayed in Figure 2f, which clearly shows a cascaded characteristic, and the thicknesses related to the PVDF and PDMS composite films are about 150 μm and 330 μm, respectively. The PVDF nanofibers with a mean diameter of 261 nm (supporting information, Figure S4a, b) are randomly distributed to form the principal sketch of composite film, in which $BaTiO_3$ particles with an average diameter of 3.689 μm (supporting information, Figure S4c, d) are well distributed within the net-shaped room of PVDF nanofibers, as shown in Figure 2g. Figure 2h demonstrates the SEM images of cross-sectional of PDMS composite film, where the indiscerptible graphite particles (2 wt%) uniformly distribute in PDMS film's interior.

Figure 2i exhibits the FTIR spectra of the as-prepared pure PVDF and PVDF composite film with 1 wt% CNT and 18 wt% $BaTiO_3$. Obvious vibration peaks at 840 cm^{-1} and 1280 cm^{-1} were observed, giving an indication of the formation of β crystalline phase [2, 8] (Figure 2j). The formation of obvious β crystalline phase therefore allow us to utilize it to fabricate piezoelectric unit in the T-HNG. Besides, the Raman spectra of additive components are well consistent with that of pure MWCNT[21] and graphite[22] (Supporting information, Figure S5a, b). FTIR spectra of pure PDMS and PDMS composite films are illustrated in Figure 2k. No remarkably difference was observed in the spectra as adding the MWCNT/graphite component, indicating that the principle ingredient close to the surface of composite film is PDMS. The symmetric and asymmetric peaks appearing at 2906 cm^{-1} and 2852~2962 cm^{-1} are due to the –CH3 stretching in ≡Si-CH_3.[23] Bands from 1258 cm^{-1} to 1412 cm^{-1} related to the stretching of C-H of –Si$(CH_3)_2$- groups were noticed[24]. In addition, two overlapping bands at 1007 cm^{-1} and 1074 cm^{-1} were also found, which are generally induced by the stretching of Si-O-Si from the main chain of PDMS. It has been previously reported that the Si-C stretching bands and Si-$(CH_3)_2$ rocking peaks were found at 825~865 cm^{-1} and 785~815 cm^{-1}, respectively, [25] which are also seen in our FTIR spectra for composite films. The relatively difference between pure PDMS and composite FTIR spectra is found at 905 cm^{-1} for which the peak becomes sharper (Figure 2l), which could be induced by the formation of Si-C bond. [23] Furthermore, the Raman spectrum (Supporting information Figure S5b, c) demonstrates the additive components in pure PVDF is MWCNT and $BaTiO_3$.[26] Although the strength of PVDF composite film has a slight decrease compared to that of pure PVDF due to the impediment of $BaTiO_3$ particles on the linkage of PVDF nanofibers (Figure 2g), the modulus of PVDF composite film is basically equivalent to that of pure PVDF (Figure 2m),

indicating the superior load-bearing capacity of net-shaped PVDF composite film. Figure 2n illustrates the stress vs. strain curves of pure PDMS and PDMS composite film. The mechanical properties of PDMS composite film have been remarkably improved, which could be explained by the strong Si-C bonding between the carbon nanoparticles and PDMS.[27]

In addition, the theoretical analysis[6, 8] has been indicated that for the dielectric layer with a given thickness, rising its relative permittivity is another way to enhance the output except boosting the surface charge density. In order to further explore it experimentally, we added the high dielectric permittivity materials such as CNT and graphite into PDMS, respectively, and used the PDMS composite film to fabricate TENGs and then evaluated the output performance of the fabricated TENGs via output voltage and surface charge density. We measured the dielectric constant and electric conductivity of the as-fabricated PDMS and PVDF composite films by using Precision Impedance Analyzer (Agilent 4294 A) and Four-Point Probes Resistivity Measurement System (4PROBES TECHTM, China), respectively. The corresponding results were shown in Figure S6, Supporting information.

According to Figure S6a, the relative dielectric constant of pure PDMS is obviously lower than that of PDMS composite films, which demonstrates that the additive CNT and graphite have an effect to improve the relative dielectric constant. In addition, the testing results of electric conductivity reveal that the concentration of CNT/graphite is still not high enough to make PDMS/PVDF conductive, see Figure S6b. Therefore, the role of CNT and graphite is to modify the dielectric constant of PDMS and PVDF films.

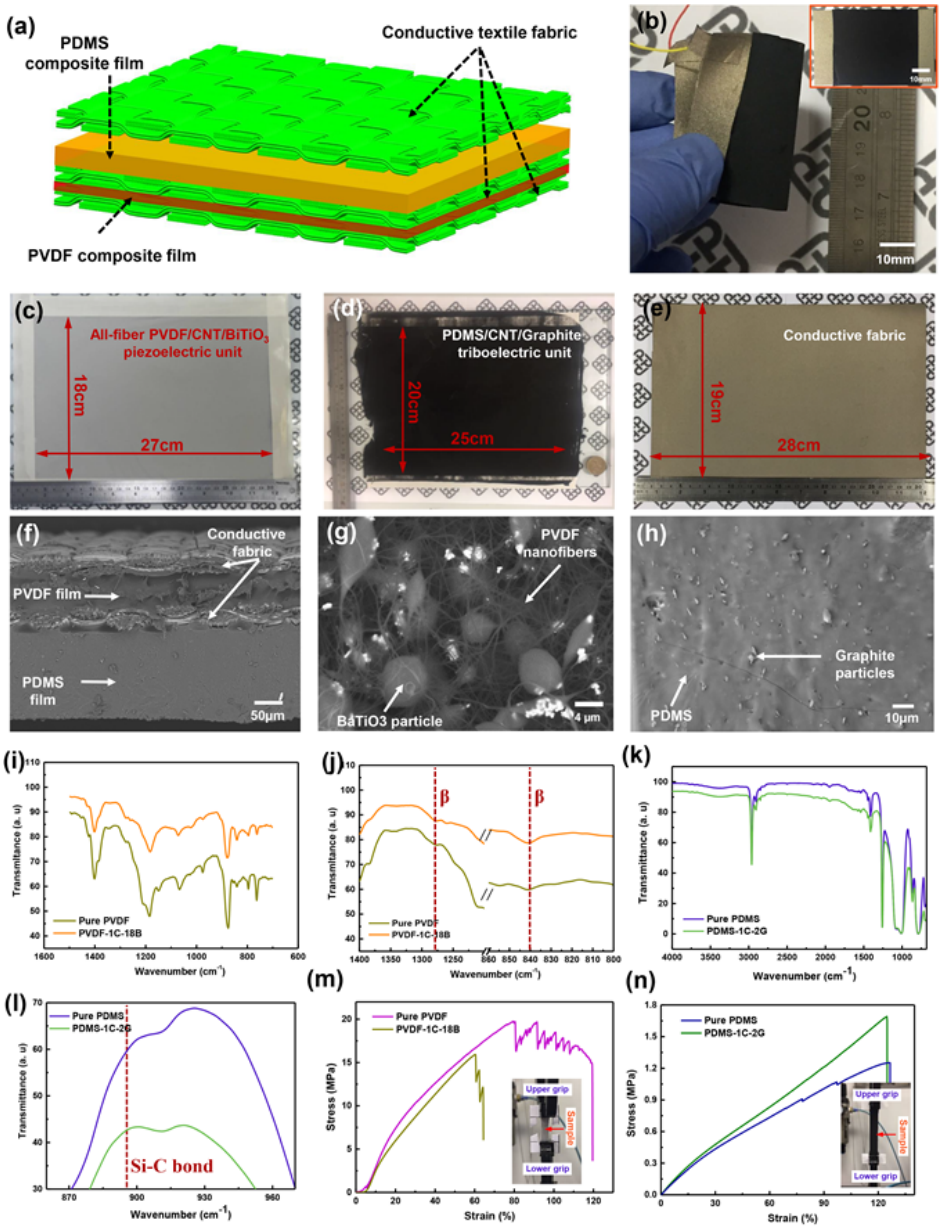

Figure 2. (a) Schematic of the T-HNG. (b) Photograph of the T-HNG. (c) Photograph of as-prepared PVDF/CNT/$BaTiO_3$ composite film. (d) Photograph of PDMS/CNT/Graphite composite film. (e) SEM image of conductive fabric electrode. (f) A cross-sectional SEM image of the T-HNG. (g) SEM image of PVDF/CNT/$BaTiO_3$ composite film. (h) SEM image of PDMS/CNT/Graphite composite film. (i) Fourier transform infrared (FTIR) spectroscopy of PVDF/CNT/$BaTiO_3$ composite film. (j) Inset displays an enlarge view of the strong vibration peaks at 840 cm^{-1} and 1280 cm^{-1} (k) FTIR spectra of pure PDMS and PDMS composite film. (l) Inset shows a magnified view of the peak at 905 cm^{-1}. (m) Stress vs. strain curves of PVDF/CNT/$BaTiO_3$ composite film. Inset shows an image of tensile test for this film. (n) Stress vs. strain curves of PDMS/CNT/Graphite composite film. Inset gives an illustration of tensile test for this film.

2.2. Optimized hybrid nanogenerator and electric performances

To the best of our knowledge, surface roughness and material components both have remarkable influences on the electric performances of nanogenerator.[5, 10] In this work, to enhance the electric performance, inexpensive sandpapers with different surface roughness (P180, P600, P1000 and P3000, P* means grit, European Standard) were used to fabricate

micro-pattern structures of PDMS composite films using a facile doctor-blading method, see the ***Experimental Section***. Likewise, conductive fillers (MWCNT and graphite) and piezoelectric ceramic particles ($BaTiO_3$) were also adopted to modify the dielectric constant and improve the piezoelectric performance, respectively. These as-mentioned impact factors on electric performances were experimentally evaluated based on T-HNG in separated tribo-/piezo-mode, and the optimized triboelectric unit and piezoelectric unit were finally obtained (Supporting information, Figure S7 and 8). The optimized TEU are composed of 1 wt% MWCNT and 2 wt% graphite, and the optimized PEU consists of 1 wt% MWCNT and 18 wt% $BaTiO_3$.

Figure 3d and e demonstrates the output voltage vs. time curves of the T-HNG fabricated by using the optimized TEU and PEU based on the connect mode I (Figure 3a). The nanogenerator can output an average peak piezoelectricity of 21.31 V and an average peak triboelectricity of 157.39 V, respectively. Nevertheless, once connecting with the triboelectric and piezoelectric units in the case of directly parallel connection mode (Figure 3b), the output average peak voltage for T-HNG shows a slight decrease by ~7% (Figure 3f). This phenomenon was also found by the previous work.[3, 8]

To elaborate this issue, Figure 3g gives the simultaneous output voltage vs. time curves of TEU and PEU in a single press-and-release process. Due to the multi-point contact induced by roughness surface of PDMS film, the output voltage for the triboelectric unit is a lot blunter than that of piezoelectric unit. Furthermore, there is a delay in the peaks in the second half cycle, which can be attributed that the tribo-charges are compensated faster than piezo-charges.[3] In the other word, a residual strain in the PVDF film still exists during the releasing process. Therefore, the output power is to some extent degraded by cancellation due to the difference in the phase of TEU and PEU. Furthermore, due to the working states of TEU and PEU are basically completely out of sync, therefore, when the TEU is activated, the effect of PEU is similar with that of capacitor in parallel mode (like a classic RC circuit). A totally similar process could also exist when the PEU is activated. Thus, the external current can be reduced, giving rise to the decrease of output voltage measured by oscilloscope, see Figure S10, Supporting information. In summary, it is of importance to design the external circuit for hybrid nanogenerators.

Figure 4 demonstrates the electric performances of T-HNG based on the optimized triboelectric unit with P3000-PDMS composite film and piezoelectric unit under the cyclic compression force of 580 N at a frequency of 3.3 Hz. The rectified average peak output voltage with an 8 MΩ resistance load is 161.66 V based on the connection mode III, which is

higher than that of the triboelectric unit, but less than that of directly adding the output voltage of triboelectric and piezoelectric units (Indivial rectified output based on PEU and TEU can be found in Figure S9, Supporting information). This finding can be attributed to the nature of measure circuit which is not entirely the case of open-circuit or short-circuit (Supporting information, Figure S10). Jung et al.[3] reported that in the case of open-circuit, the peak output performance (voltage) of hybrid nanogenerator is almost close to that of triboelectric unit, but in the case of short-circuit, the peak output performance (current) is completely added to the triboelectric and piezoelectric output. Additionally, according to the enlarged view of the output voltage in Figure 4a, although there is an obvious phase delay between the output from TEU and PEU, the output voltages induced by individual unit both have an effective contribution to the comprehensive output voltage of hybrid nanogenerator thanks to the two full-wave bridge diodes circuits.

Moreover, external resistor load matching, charging capacity and long-term stability for the T-HNG has also been investigated, shown in Figure 4b-f. Figure 4b exhibits the voltage on the capacitor vs. time curve when a 100 μF capacitor was charged from T-HNG based on the connection mode III. The curve represents the charging of 100 μF capacitor to a voltage of ~5.5 V in 500 s, driving a green LED lighting.

With an increase in the load resistance, the maximum current decreases due to heavier blocking by larger external resistance, while the maximum voltage across the resistor load has an opposite trend. The instantaneous output power calculated by $W = I_{peak}^2 \times (R_o + R_i)$ is ~2.22 W/m^2 at an external load of 20 MΩ (Figure 4d), where R_{in} and R_{out} are the resistance of high-voltage probe and external resistance, see Figure S10, Supporting information. Compared with previous nanogenerators with a micropatterned plastic film,[7] the value is nearly enhanced by one order of magnitude. Besides, the T-HNG generally maintains its output voltage at the end of the 5, 000 cyclic compression at a frequency of 3.3 Hz (Figure 4e).

2.3. Application of the optimized hybrid nanogenerator

To demonstrate the applications of the T-HNG for mechanical energy harvesting, we first fixed the T-HNG on a four-spring device to harvest mechanical energy. Figure 5 exhibits the T-HNG is capable of directly powering of up to 150 LEDs to form a “STAR” logo, and 100 green LEDs. A 100 μF capacitor was charged for about 500 cycles, and the stored energy readily powered the display device and calculator (Figure 5d and e).

Being flexible, large-scale and wearable energy harvesting devices for human motion, we integrated the T-HNG at various parts of human body, i.e. hands, shoes, coats and trousers,

to demonstrate the applications (Figure 6). To harvest energy from human motion, two parts in the T-HEG with an effective area of 4.5 cm×5 cm are respectively pasted onto the relative surface of gloves, making up a power generating glove that can generate a pulse voltage with the maximum value of ~55 V, instantaneously lighting up 15 LEDs (Figure 6a). Figure 6b illustrates a power generating shoe which reaches more than ~80 V average maximum output voltage (10 μA, with 8 MΩ external resistor), driving 15 LEDs instantaneously. Because each footstep can generate one cycle of voltage, the T-HNG could also work as active sensor which calculates the number of footsteps. The T-HNG can be integrated in clothes, such as trousers and coats to easily harvest energy by patting, see Figure 6c, d. Figure 6c demonstrates the voltage generated by a power generating trouser, which approaches about 45 V pulse voltage. Figure 6d also exhibits a power generating coat, which can simultaneously drive 15 LEDs in the case of ~55 V pulse voltage. As mentioned above, the proposed T-HNG is an extremely promising power supply for wearable devices.

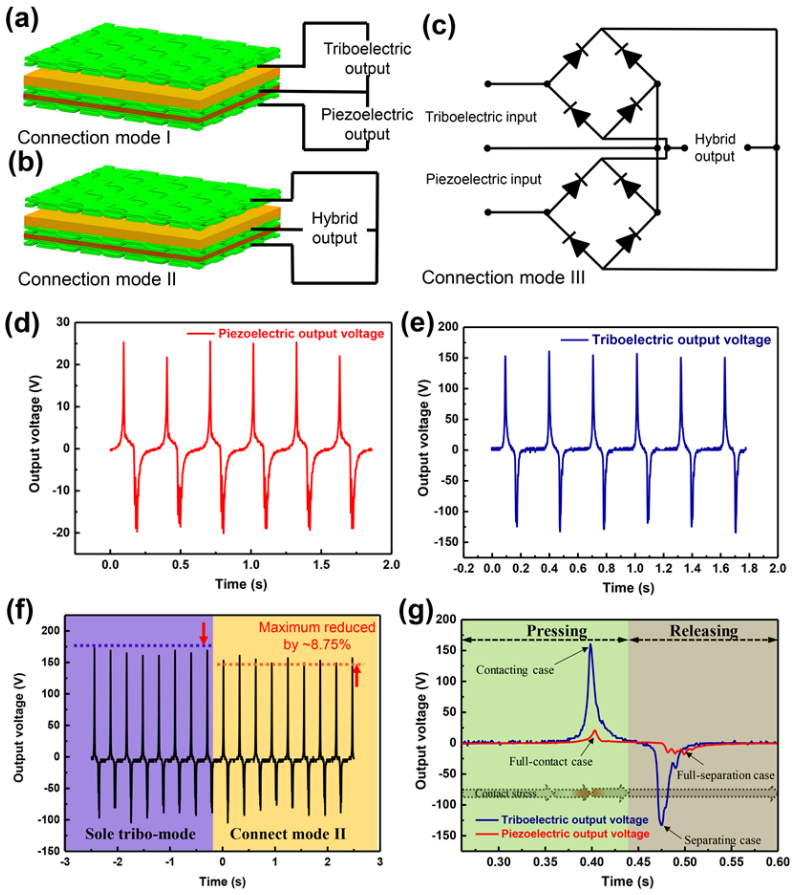

Figure 3. Influence of external circuit on the output voltage of hybrid nanogenerator. (a) Individual measurement circuit without rectification for piezoelectric and triboelectric units (Connection mode I). (b) Concurrent measurement circuit without rectification for hybrid nanogenerator based on directly parallel connection mode (Connection mode II). (c) Concurrent measurement circuit for hybrid nanogenerator based on two full-wave bridge diodes circuits (Connection mode III). (d-f) Output voltage vs. time curves of PEU, TEU and T-HNG. (g) Output voltage vs. time curve of TEU. (f) Output voltage vs. time curves of PEU and TEU, measured individually in a single press-and-release cycle.

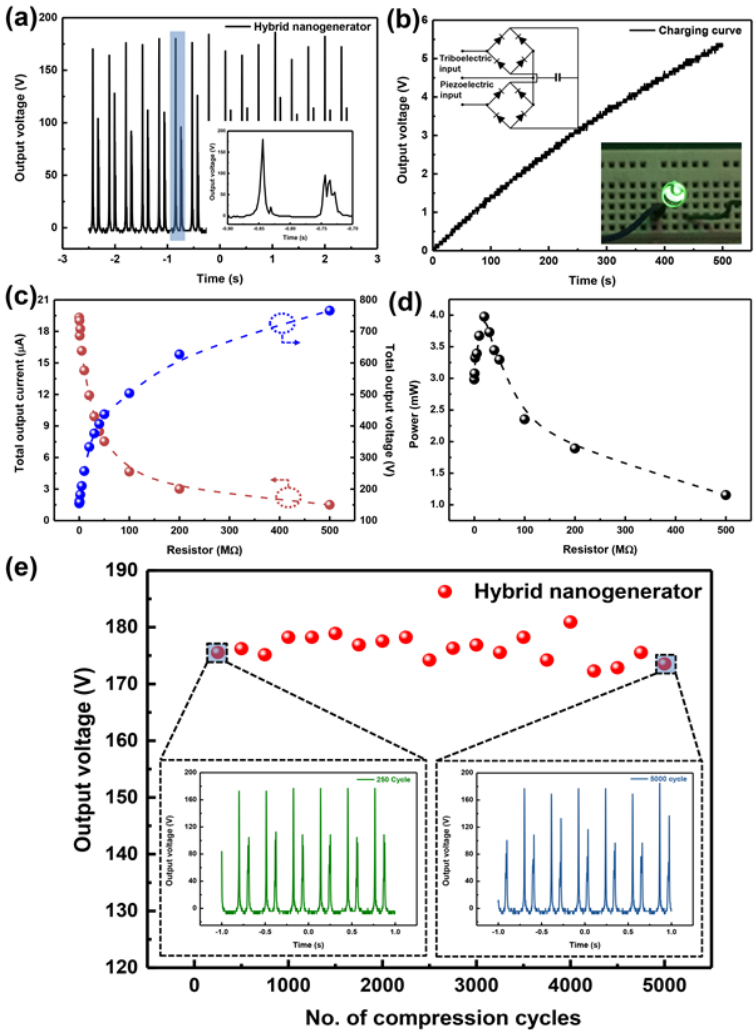

Figure 4. Electric performance of T-HNG. (a) Representative output voltage generated by the optimized T-HNG. The inset illustrates an enlarged voltage vs. time curve. (b) Charging curve for 100 μF capacitor as a function of time. Left inset shows the schematic of capacitor charging circuit using T-HNG, and right inset exhibits powering of a LED by a charged capacitor. (c) Total output current and voltage with varying load resistors. (d) Power output as a function of varying resistors. (e) Long-term stability of T-HNG under the 5000 compression cycles (load: 598 N, frequency: 3.3 Hz). The inset images show the output voltages of T-HNG at the cycles of 250 and 5000, respectively.

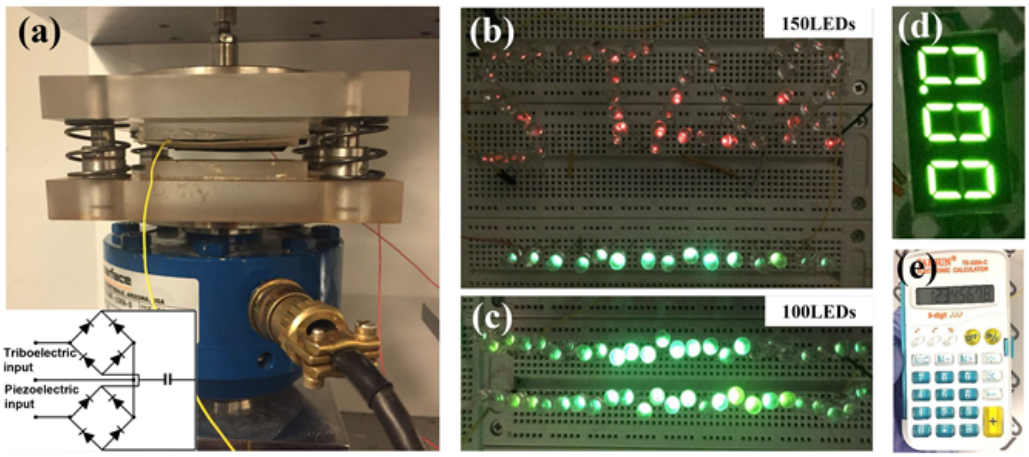

Figure 5. Photographic image of application of the T-HNG assisted with a four-spring device. (a) Four-spring device driven by ZX-A03. Inset shows the two full-wave bridge circuit. (b) A "STAR" shape pattern composed by 150 LEDs (50 green LEDs and 100 red LEDs) were powered by a 4.5 cm×5 cm T-HNG (load: 598 N, frequency: 3.3 Hz). (c) 100 green LEDs were lighted by the T-HNG. (d-e) Application of display device and calculator.

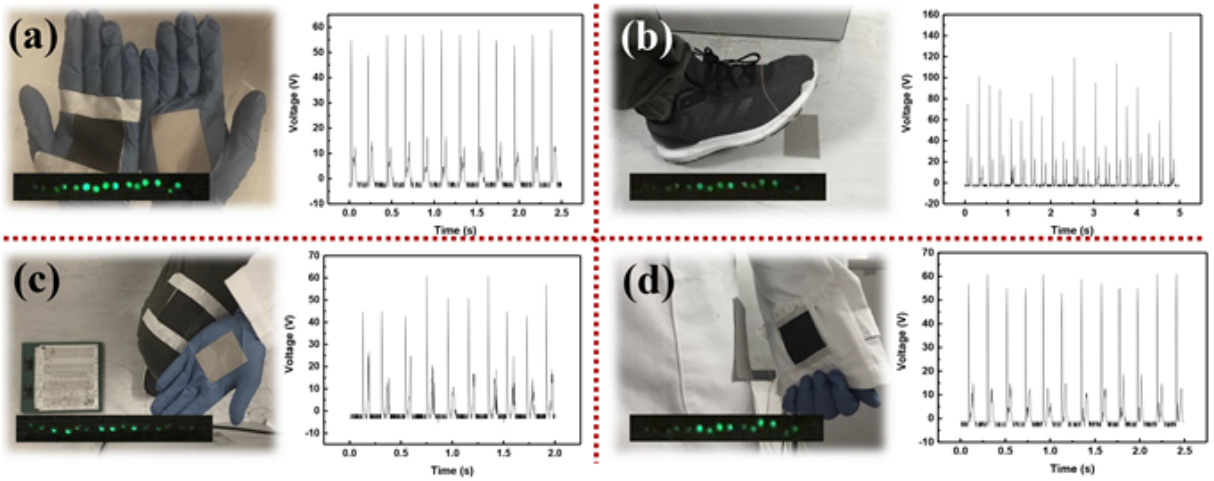

Figure 6. Photographic image of the T-HNG fixed at various positions of human body and the corresponding output voltage obtained from the two full-wave bridge diodes circuits. (a) A pair of power generating gloves that could harvest energy from claps and light up 15 LEDs and output the maximum voltage of ~ 55 V. (b) A T-HNG integrated in a shoe harvesting energy from footsteps, driving 15 LEDs working. The maximum output voltage approaches to 150 V, which is larger than that obtained by clapping due to higher external load. (c)~ (d) Power generating trouser and coat harvesting movement energy by patting.

3. Discussion

3.1. Operation mechanism of the optimized T-HNG

Figure 7 elaborates the operation mechanism of this novel T-HNG, which is relevant to the comprehensive result of piezoelectric, triboelectric and electrostatic effects. The cascaded sequence from top to bottom includes: the triboelectric unit comprising electrode 1 (ED 1), optimized PDMS composite film and electrode 2 (ED 2), and the piezoelectric unit consisting of ED 2, optimized PVDF composite film and electrode 3 (ED 3). The ED 2 is shared with TEU and PEU, and the ED 1 stuck to an acrylic plate that can move up and down controlled by the keyboard life tester, see Figure 7a. One periodic motion of ED 1 can be investigated and divided into eight cases: (i) t_0 (the ED 1 moves to the highest location, viz. $x = X_{\max}$); (ii) Δt_1 (from t_0 to t_1, the ED 1 moves from $X_{\max}$ to the initial contact location of x_s); (iii) t_1 (the ED 1 moves to $x = 0$); (iv) Δt_2 (from t_1 to t_2, the ED 1 moves from x_s to the lowest location, namely $x = X_{\min}$); (v) t_2 (the ED 1 moves to the lowest location); (vi) Δt_3 (from t_3 to t_4, the ED 1 moves back from $X_{\min}$ to the location of x_s); (vii) t_3 (the ED 1 moves to the location of $x = x_s$); (viii) Δt_4 (from t_3 to t_4, the ED 1 moves back from x_s to the highest location of $x = X_{\max}$); t_4 is the case that the ED 1 returns to the case of (i). Among them, the influence of compressive stress loaded by external load on the piezoelectric unit only exists during the period of Δt_2 and Δt_3, respectively. The regulation of motion and external load with the variation of time can be found in Figure 7b.

After sufficient contact, equal charges with opposite polarity induced by triboelectric effect uniformly distribute on the two contact surfaces of ED 2 and PDMS.[8, 10, 28] In the case of t_0, the tribo-charges in ED 1 fully flow to the ED 2 though the external circuit, due to the electrostatic effect. Subsequently, as the ED 1 starts moving back during the case of Δt_1, the tribo-charges flow though the external circuit from ED 1 to ED 2 (Figure 7d(ii)). Until that the ED 1 and PDMS film are fully contact, the charges thoroughly flow back from ED 1 to ED 2 (Figure 7d(iii)). Likewise, due to the diminishment of compressive stress inside PEU (the gap inside polarized dipoles remains constant), no charges output induced by piezoelectric effect between EDs 2 and 3 from t_0 to t_1. During the case of Δt_2, the piezoelectric unit will be activated induced by the compressive load (the gap inside polarized dipoles gradually reduces), driving the output of piezo-charges flowing from ED 3 to ED 1 (Figure 7d(iv)). Owing to the fully contact state, there is no tribo-charges flowing between the ED1 and ED 2. In the case of t_2, a new saturation state with regard to piezoelectric effect will be achieved, at which the piezo-charges inside EDs 2 and 3 reach the maximum value[14] (Figure 7d(v)). Afterwards, during the stage of Δt_3, the piezoelectric charges reversely output until that the compressive stress inside PEU is fully released (Figure 7d (vii)), when the gap inside polarized dipoles retures back the orignial position. Subsequently, the contact surfaces begin to separate, the tribo-charges driven by electrostatic effect flow back from the ED 2 to ED 1 (Figure 7d(viii)). Ultimately, the ED 1 again moves to the highest location corresponding to the case of t_0, at which the tribo-charges are fully transferred from ED 2 to ED 1. In conclude, the T-HNG achieves a contact-separate cycle, driving the electrons induced by triboelectric and piezoelectric effects flowing back and forth among the three electrodes though the external circuit.

Additionally, the discussion with regard to the polarization process for PVDF composite film has been given in our previsous work,[2] and the corresponidng mechanism can be found in ***Section S1***, supporting information.

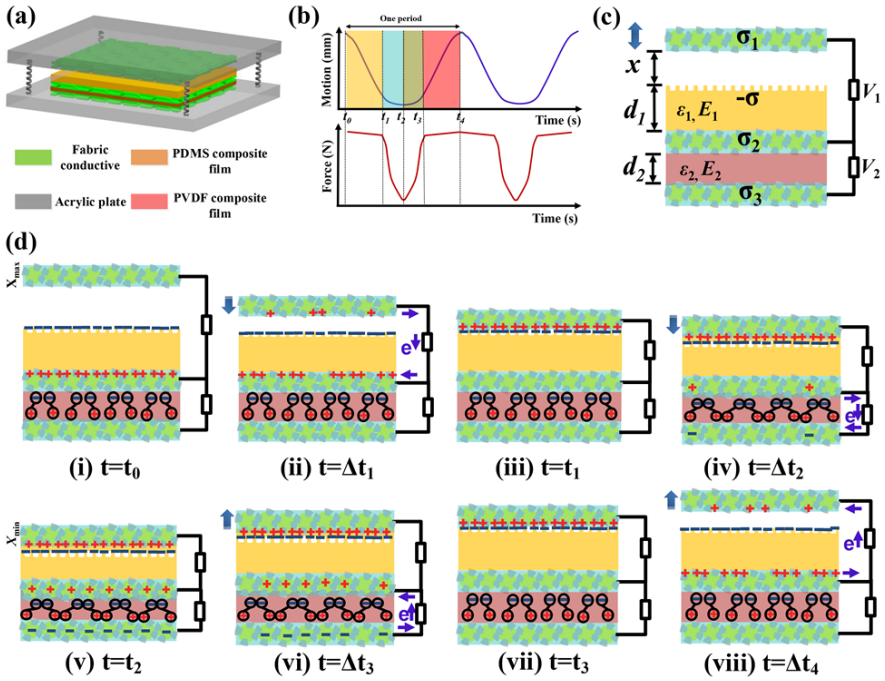

Figure 7. Operation mechanism of the contact-separation mode T-HNG. (a) Schematic illustration of T-HNG assisted by a four-springs rigid device. (b) External load and motion regulations as a function of time. (c) Electric and geometric parameters. (d) Sketches that illustrate the electricity generation process in a full period.

3.2. Finite element simulation for T-HNG

To obtain a more unambiguous understanding about the operation mechanism of T-HNG mentioned in this work, finite element simulation using COMSOL was employed to qualitative analyze the charge-separation-induced potential difference as well as corresponding stress distribution. Due to the same configuration perpendicular to the cross-section area, only a 2D analysis mode was adopted in COMSOL software. The constructed model has the same structure and size with the real device along the thickness direction (Figure 2a). However, since the surface of real PDMS composite film has substantial micro-pattern structures, these structures are assumed to be rectangular to simulate the roughness surface. Finally, a representative 2D model with a width of 1.48 mm and a bumpy surface formed by 19 rectangular configurations was built. The structure as well as the corresponding dimensions were shown in **Figure 8a**. After sufficient contact, the positive triboelectric charges of the ED 1 are equal to the negative charges retained on the PDMS composite film, as mentioned above. Therefore, it is reasonable to assume that the two contact surfaces uniformly distribute equal tribo-charges that are given by ±1 μQ. In addition, this device is in open-circuit case, which means no electrons transfer among the three electrodes.

As mentioned in ***Section 3.1***, five typical cases in a half period are considered, namely $t_0\,(x = X_{\max})$, $\Delta t_1\,(x = X_{\max} \sim x_s)$, $t_1\,(x = x_s)$, $\Delta t_2\,(x = x_s \sim X_{\min})$, and $t_2\,(x = X_{\min})$. At the stage of t_0, the maximum open-circuit voltage approaches 5650 V at the gap of 0.2 mm (Figure 8b(i)),

which will keep decreasing when the gap between the two contact surfaces gets larger[19]. When the ED 1 moves to the location of 0.1mm, the corresponding voltage is only 3520 V (Figure 8b(ii)). This simulation result in the case of open-circuit voltage is well consistent with the results obtained by the theory of electrical field in capacitance. Interestingly, the values of maximum compressive stress inside PEU are fairly low, only 0.0823 MPa (x = 0.2 *mm*) and 0.0447 MPa (x = 0.1 *mm*). The finding given by simulation indicates during this process, the piezoelectric effect is unavailable, verifying the conclusion mentioned above that after separating between the two contact surfaces, the flowing charges originate from the triboelectric effect, rather than piezoelectric effect, and therefore the charges mostly flow though the external circuit between EDs 1 and 2. Once the two surfaces fully contact, viz. $x = x_s$, there is no potential difference generated (Figure 8b(iii)), because of the diminishment of piezoelectric effect and electrostatic balance. When the ED 1 continually moves to the location of x = -0.015 *mm*, the maximum and minimum open-circuit voltages distribute the both sides of PEU, demonstrating that the piezoelectric effect is active. In this moment, the corresponding stress and voltage reach to 20.1 MPa and 3.09 V, respectively (Figure 8b(iv)). This compressive loading makes the gap of polarized dipoles resduce. With the increase of compressive stress inside PEU, the output voltage of T-HNG generally rises unit to the maximum value of 40.2V, when the ED 1 moves to the lowest location (Figure 8b(v)). As soon as the ED 1 is reverted to move, the open-circuit voltage induced by triboelectric and piezoelectric effects will have a fully reverse trend, up to the stage of $x = X_{\max}$.

Figure 8c quantitatively depicts the variation trends of the maximum open-circuit voltage and contact stress as a function of distance x . The contact stress dramatically decreases with the increase of distance from 40 MPa to 0 MPa, which corresponds a remarkable rise of maximum open-circuit voltage after that the distance is larger than zero. The voltage rises monotonically with the increase of distance curve. Nevertheless, when the distance is large enough, the raise speed of it tends to be slow and the value approaches to its saturation value. This result was also obtained by the previous theoretical investigation.[29] and experimental verification. [17] In addition, in the case of open circuit, the tribo-charges are much larger than the piezo-charges, which is also consist with the previous conclusion[30]. Figure 8d illustrates the open-circuit voltage contour of piezoelectric units comprising of PVDF with 18 wt% $BaTiO_3$ and pure PVDF at the stage of $x = X_{\min}$. The maximum open-circuit voltage for the PVDF composites is larger than that for the pure PVDF, giving a quantitatively indication of the enhancement effect of $BaTiO_3$ particles. Additionally, the value for PVDF composites is

6.37 V, which happens to be equal to the entire voltage shown in Figure 8b(v) in the same case. This finding unambiguously reveals that in the case of t_0, the piezoelectric unit is the principle working unit in the T-HNG, after the two contact surfaces achieve the fully contact state. Figure 8e exhibits the local images of open-circuit voltage distribution for T-HNG in the case of $x = 0.01\ mm$. Compared with the maximum open-circuit voltage values, the value for the PDMS with roughness surface is obviously higher than that for the flat PDMS, enhanced by ~40 V, which can be attributed to the increase of gap between the two contact surfaces.

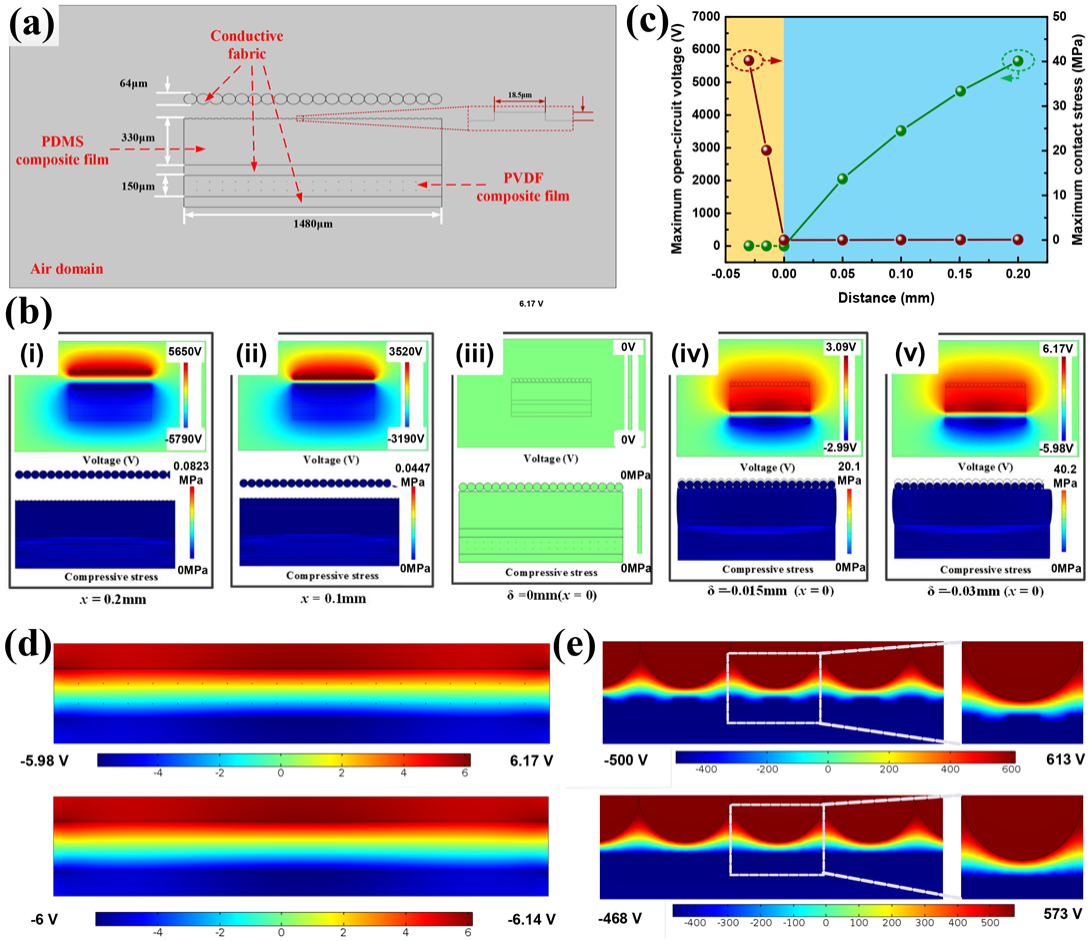

Figure 8. Finite element simulation of T-HNG in contact mode. (a) Schematic diagram of the model for the calculation. (b) Finite element simulation of the potential distribution in the T-HNG for the different compression and separation distances. (c) Maximum open-circuit voltage and contact stress as functions of distance. (d) Voltage distributions of piezoelectric units based on PVDF with 18 wt% $BaTiO_3$ and pure PVDF. (e) Voltage distributions of triboelectric units with flat and micro-pattern configurations. Insets show that highly magnified images of the corresponding local regions used in the simulation.

3.3. Theoretical analysis for T-HNG

To further understand the operatiton mechanism and output characteristics of T-HNG, a systematically theoretical analysis was carried out. The schematic illustration of structure and relevant material symbols are consistent with the one shown in Figure 7 c. Before discussing, some assumes must be given as follow: (i) the tribo-charges are uniformly distributed on the contact surface with negligible decay[31]; (ii) Ideally, the triboelectric and piezoelectric unit

have an independent circuit[8], meaning that the charges induced by each unit are not coupled, see Figure 7c. (iii) The electric potentials in Figure 7c regards as a close loop of circuit, which means the Eqation (1) and (2) can be satisfied.

$$V_{\mathrm{a}} + V_{\mathrm{PD}} + V_1(t) = 0 \tag{1}$$

$$V_{\mathrm{PV}} + V_2(t) = 0 \tag{2}$$

where V_{a}, V_{PD} and V_{PV} are the voltage of the air, PDMS and PVDF domains. $V_1(t)$ and $V_2(t)$ are the voltage of external resistors.

To quantitatively elaborate the output characteristics of T-HNG more explicitly, a conductor-to-dielectric triboelectric nanogenerator in a contact-separate mode is firstly investigated based on the same structure, material and dimension as the triboelectric unit in our T-HNG (Detailed process can be found in ***Section S10***, Supporting Information. The corresponding *V*-*Q*-*x* relationship can be obtained, namely

$$R\frac{\mathrm{d}Q}{\mathrm{d}t} + \left(d_r + x(t)\right)\frac{Q}{S\varepsilon_0} - \frac{\sigma}{\varepsilon_0}x(t) = 0 \tag{3}$$

where R is external resistor; d_r is effective thickness constant ($d_r = d/\varepsilon_r$), d and ε_r are thickness and relative permittivity; $x(t)$ is separation distance; S is the contact area; ε_0 is vacuum permittivity. As for the T-HNG, due to the independent connection mode between TEU and PEU, the theoretical equation of TEU in T-HNG can be considered the same as that of the mentioned triboelectric nanogenerator, in which the PEU can be similarly regarded as the corresponding electrode of the nanogenerator, see Figure 7. Therefore, the theoretical equation of TEU is directly capable of describing as the following formation, viz.

$$R_1\frac{\mathrm{d}Q_1}{\mathrm{d}t} + \left(d_{r1} + x_1(t)\right)\frac{Q_1}{S\varepsilon_0} - \frac{\sigma}{\varepsilon_0}x_1(t) = 0 \tag{4}$$

Where R_1 and d_{r1} are the external resistor and relative permittivity for TEU; $x_1(t)$ is the movement equation of ED 1 during the time of Δt_1 , Δt_4 . σ is the surface charge density; Q_1 is the amount of transferred charges in the ED 1. In addition, the initial condition is given in case of $t = t_0 = 0$ (Figure 7b), viz.

$$\begin{cases} Q_1(t=0) = 0 \\ Q_2(t=0) = \sigma S \\ Q_3(t=0) = 0 \end{cases} \tag{5}$$

where Q_2 and Q_3 is the amount of transferred charges on the EDs 2 and 3. Thus, when triboelectric unit is available to work, by combining the initial conditions in Eqation (5), the Eqation (4) can be solved analytically as

$$Q_1(t) = S\sigma - e^{-\int_0^t \frac{d_r + x_1(\tau)}{R_1 S\varepsilon_0} \mathrm{d}\tau} \left(S\sigma + \int_0^t \frac{\sigma x_1(\tau)}{R_1 \varepsilon_0} e^{\int_0^\tau \frac{d_r + x_1(\gamma)}{R_1 S\varepsilon_0} \mathrm{d}\gamma} \mathrm{d}\tau \right), \quad (t \in [\Delta t_1, \Delta t_4]) \tag{6}$$

In addition, when the triboelectric surfaces fully contact with each other once again, the ED 1 will continue to move down and up during Δt_2 and Δt_3, at which the piezoelectric unit is activated (Figure 7(d)). In accordance with Eqation (2) and Ohm' law, we can obtain

$$E_2 d_2(t) + R\frac{\mathrm{d}Q_2}{\mathrm{d}t} = 0 \tag{7}$$

where Q_2 is the amount of transferred charges between EDs 2 and 3; E_2 and $d_2(t)$ are the electric field strength and thickness of PVDF layer, respectively. Here, the $d_2(t)$ can be expressed as

$$d_2(t) = d_0 - x_2(t) \tag{8}$$

Where d_0 is the original thickness of PVDF layer; $x_2(t)$ is the movement equation of ED 1 during the time of Δt_2, Δt_3. According to Gauss's law, E_2 can be expressed as:

$$E_2 = \frac{Q_2}{S\varepsilon_{r2}\varepsilon_0} \tag{9}$$

where ε_{r2} is the relative permittivity of PVDF layer. Thus, substitute Eqation (8) and (9) to Eqation (7), we can obtain

$$\frac{\mathrm{d}Q_2}{\mathrm{d}t} + \frac{d_0 - x_2(t)}{RS\varepsilon_{r2}\varepsilon_0} Q_2 = 0 \tag{10}$$

To be simplified, the initial time for the derivation process of piezoelectricity equation is redefined as $t = 0$, because of fully independent process between triboelectricity and piezoelectricity (only definition, in fact, $t = t_1 \neq 0$, see Figure 7b). Thus, the corresponding initial conditions can be obtained

$$\begin{cases} Q_1(t=0) = 0 \\ Q_2(t=0) = Q_0 \\ Q_3(t=0) = Q_0 \end{cases} \tag{11}$$

As Eqation (10) is a first-order differential equation, it can be analytically solved by combining the initial conditions (Eqation (10)). Thus, the regulation equation for piezoelectric effect is given as

$$Q_2 = Q_0 e^{-\int_0^t \frac{d_0 - x_2(\tau)}{R_2 S\varepsilon_{r2}\varepsilon_0} \mathrm{d}\tau}, \quad (t \in [0, \Delta t_2 + \Delta t_3]) \tag{12}$$

In conclusion, the output current and voltage across the resistor can be depicted by the following equations, respectively.

$$I(t)=\frac{\mathrm{d}Q(t)}{\mathrm{d}t}=\begin{cases}-\dfrac{\sigma x_1(t)}{R_1\varepsilon_0}+\dfrac{d_r+x_1(t)}{R_1S\varepsilon_0}e^{-\int_0^t\frac{d_r+x_1(\tau)}{R_1S\varepsilon_0}\mathrm{d}\tau}\left(S\sigma+\int_0^t\dfrac{\sigma x_1(\tau)}{R_1\varepsilon_0}e^{\int_0^\tau\frac{d_r+x_1(\gamma)}{R_1S\varepsilon_0}\mathrm{d}\gamma}\mathrm{d}\tau\right), & \left(t\in[\Delta t_1,\Delta t_4]\right)\\ -\dfrac{(d_0-x_2(t))Q_0}{RS\varepsilon_{r2}\varepsilon_0}e^{-\int_0^t\frac{d_0-x_2(\tau)}{R_2S\varepsilon_{r2}\varepsilon_0}\mathrm{d}\tau} & ,\quad \left(t\in[0,\Delta t_2+\Delta t_3]\right)\end{cases} \tag{13}$$

$$V(t)=RI(t)=\begin{cases}-\dfrac{\sigma x_1(t)}{\varepsilon_0}+\dfrac{d_r+x_1(t)}{S\varepsilon_0}e^{-\int_0^t\frac{d_r+x_1(\tau)}{R_1S\varepsilon_0}\mathrm{d}\tau}\left(S\sigma+\int_0^t\dfrac{\sigma x_1(\tau)}{R_1\varepsilon_0}e^{\int_0^\tau\frac{d_r+x_1(\gamma)}{R_1S\varepsilon_0}\mathrm{d}\gamma}\mathrm{d}\tau\right), & \left(t\in[\Delta t_1,\Delta t_4]\right)\\ -\dfrac{(d_0-x_2(t))Q_0}{S\varepsilon_{r2}\varepsilon_0}e^{-\int_0^t\frac{d_0-x_2(\tau)}{R_2S\varepsilon_{r2}\varepsilon_0}\mathrm{d}\tau} & ,\quad \left(t\in[0,\Delta t_2+\Delta t_3]\right)\end{cases} \tag{14}$$

where the movement equation of ED 1 can be expressed as

$$\begin{cases}x_1(t)=A_1\sin(\omega t+\varphi)+A_1, & \left(t\in[\Delta t_1,\Delta t_4]\right)\\ x_2(t)=A_2\sin(\omega t+\varphi_1)+A_2, & \left(t\in[0,\Delta t_2+\Delta t_3]\right)\end{cases} \tag{15}$$

where A_0 and A_1 are the amplitude of the movement equation of ED 1; φ_1 and φ_2 are the initial phase angles; ω is the angle velocity. In according with the experimental conditions, the parameters utilized in Eqation (14) and (15) are listed in **Table 1.**

Table 1 Theoretical analysis parameters

Symbol	Value
External resistor in the triboelectric circuit, R_1	10 [MΩ]
External resistor in the piezoelectric circuit, R_2	10 [MΩ]
Areal sizes of the PDMS and PVDF layers, S	22.5 [cm^2]
Thickness of PDMS layer, d_1	330 [mm]
Thickness of PVDF layer, d_2	150 [mm]
Vacuum permittivity, ε_0	8.854×10^{-12} [F m^{-1}]
Relative permittivity of PDMS layer, ε_{r1}	3.4
Relative permittivity of PVDF layer, ε_{rP}	7.6
Relative permittivity of $BiTiO_3$ layer, ε_{rB}	1251.3
Amplitude of the movement equation in $(\Delta t_1,\Delta t_4)$, A_0	5 [mm]
Amplitude of the movement equation in $(\Delta t_2,\Delta t_3)$, A_1	0.5 [mm]
Initial phase angle of the movement equation in $(\Delta t_1,\Delta t_4)$, φ_1	π/2 [rad]
Initial phase angle of the movement equation in $(\Delta t_2,\Delta t_3)$, φ_2	π/2+2π/5 [rad]
Angle velocity, ω	2πf [rad s^{-1}]
Frequency, f	3.3 [Hz]
Initial surface charges density induced by triboelectric effect, σ_0	15 [μC m^{-2}]
Initial surface charges induced by piezoelectric effect, Q_0	5×10^{-3} [μC]

Note: we neglect the relative perimittivity of 1 wt% MWCNT, and the Relative perimittivity of PVDF/1 wt% CNT/18 wt% $BiTiO_3$ ε_r can be simply calulated by weight average, namely: $\varepsilon_r=0.82\varepsilon_{rP}+0.18\varepsilon_{rB}$

Figure 9 illustrates the comparison results based on experiments and theoretical models in Eqation (14). When the triboelectric effect is activated, viz. $t \in [\Delta t_1, \Delta t_4]$, the output voltage as a function of time can be quantitatively predicted by the upside expression in Equation (14), where the initial point of experimental curve has been moved into the coordinate original point. The predicted maximum voltage value and time-voltage curve shape induced by triboelectricity both agree well with the corresponding experimental results, see Figure 9a. When the piezoelectric effect is activated, viz. $t \in [0, \Delta t_2 + \Delta t_3]$, the downside expression in Equation (14) can be used to predict the output voltage behavior, in which the initial point of piezoelectric output response has been also translated to the origin of coordinate system. However, indeed, there is a relatively large error between the experimental and prediction values based on the piezoelectric unit, see Figure 9b. More specifically, the predicted time-voltage curve has a wider waveform but lower valley in the second-half period in comparison with the related experimental curves output from piezoelectric unit. Therefore, the explicit expressions in Equation (14) are basically capable of qualitatively describing the triboelectric and piezoelectric output voltages of hybrid nanogenerator.

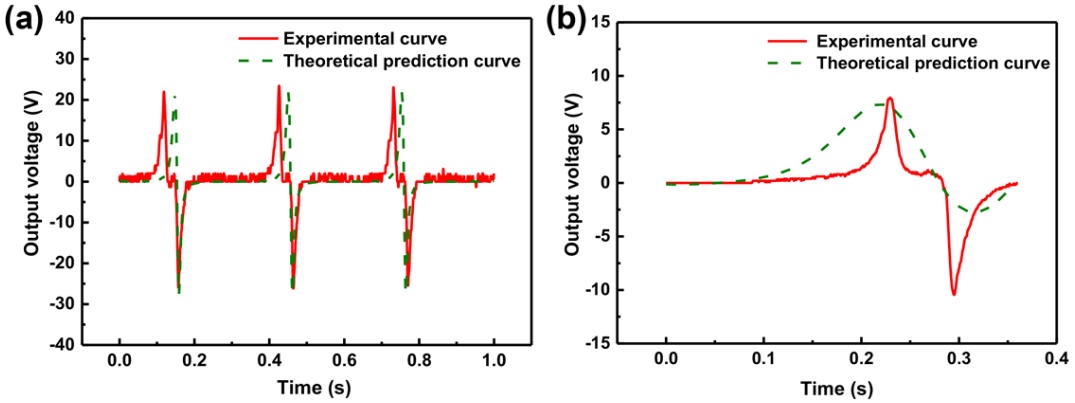

Figure 9. Comparison between the experimental and theoretical results. (a) Triboelectric output voltage curves. (b) Piezoelectric output voltage curves.

It is noted that although the cascaded mode in term of triboelectric unit is similar with the previous theoretical work by us,[8] the derivation of the corresponding explicit analytical equation for voltage as expressed in Eqation (14), is different. Here we take the previous conclusion that the two units in series are adding to each other without any synergetic effect. The piezoelectric unit is equal to the total output subtracted by that from the triboelectric unit. Thus the piezoelectric explicit equation appears different. In addition, intriguing, the open-circuit voltage V_O can be derived from the Eqation (4) into the following explicit form, namely

$$V_O = \frac{\sigma}{\varepsilon_0} x_1(t) \tag{16}$$

According to the Eqation (16), when the σ and ε_0 are constant, the response of V_O keeps synchronized with that of $x_1(t)$. The finding with regard to V_O is well coincided with the simulated open-circuit voltage vs. time curve shown in Figure 8c, giving an indication of reasonable simulation and analytic model proposed in this work.

4. Conclusion

In summary, we have designed, fabricated, characterized and theoretically investigated a novel textile hybrid nanogenerator with cascaded triboelectric and piezoelectric units. An as-spun PVDF composite nanofiber nonwoven layer and a free-standing PDMS composite layer with a micro-structured surface configuration, coated on an inexpensive sandpaper substrate, acted as the active layers. The resultant nanogenerator demonstrates a high bending flexibility up to ~180º, a large-area up to ~19 cm×27 cm before being cut into small samples and wearability in activities like hand clapping, walking and patting. The T-HNG can be fabricated by facile solution processes, in which the piezoelectric layer does not require further polarization and the micro-structured triboelectric layer can be directly peeled off from the sandpaper substrate. The optimized T-HNG with 4.5 cm×5 cm area is capable of outputting the peak voltage of 161.66 V and electric power density of 2.22 W/m^{-2}, which can directly drive 150 LEDs. More importantly, working mechanism of such T-HNG can be qualitatively analyzed by finite element simulation and quantitatively predicted by a new explicit theoretical model proposed in this work.

5. Experimental Section

Preparation of PVDF, PDMS composite film and hybrid nanogenerator: Figure 1 displays the schematic diagram of the fabrication process of hybrid nanogenerator. The flexible and large-scale PVDF composite film was prepared by a facile electrospinning technology, as shown in Figure 1a, where the ingredients of as-prepared film are composed of PVDF powder, $BaTiO_3$ powder and MWCNT. First, 18 wt% PVDF powder (the Hong Kong Polytechnic University) was thoroughly dissolved in the mixture of acetone and *N*, *N*'-dimethyformamide and (mass ratio, 1:4) at ~80℃ to prepare the PVDF electrospinning solution. Second, the 1 wt% MWCNT (Nanjing XFNANO Materials TECH Co., Ltd, 12 nm average diameter and 3~12 μm length) and $BaTiO_3$ particles (wt% of $BaTiO_3$ in PVDF: 6%, 12%, 18% and 24%) were simultaneously added to the mixture solution (Figure 1a(i)). Subsequently, the as-prepared solution was placed into a 20 mL plastic syringe with a

stainless steel nozzle of 1 mm in diameter for electrospinning (Figure 1a(ii)). Here, a piece of conductive fabric electrode covered on the rotating collector in advance (Figure 1a(ii)). The voltage was set 28 kV positive voltage and 4 kV negative voltage, and the tip-to-collector distance was ~10 cm. (Figure S1 in Supporting information gives the detailed fabrication process of PVDF composite film)

The flexible and large-scale PDMS composite film with a roughness surface structure was fabricated by a doctor-blading method. Monomers for PDMS and cross-linking agent (XE15-645, Momentive) were fully mixed with a mass ratio of 1:1 to prepare PDMS solution. Subsequently, 1 wt% MWCNT and graphite particles (Nanjing XFNANO Materials TECH Co., Ltd, 30 nm average diameter) were together added into the as-prepared PDMS solution, and were thoroughly dispersed with petroleum ether via magnetic stirrer for 1 h (Figure 1a(iv)). After dissolving sufficiently, the solution was transferred to the sandpaper with the area size of ~25 cm×20 cm fixed on a glass mold to form the surface micropattern for PDMS composite film (Figure 1a(v)). Afterwards, the mold was placed into an oven at 80 for 4 h, and the solidified film was detached from the glass mold. Figure 1b, c show the surface morphology and roughness of the PDMS composite film, which demonstrates that the micro-pattern hole configuration is capable of uniformly distributing on the surface of film assisted by inexpensive sandpaper. Interestingly, this free-standing composite film can be perfectly peeled off from the sandpaper substrate without extra work (Supporting information Figure S2b). (Figure S2 in Supporting information gives the detailed fabrication process of PDMS composite film)

Finally, the PVDF composite film and PDMS composite film were inseparably cascaded together by using the same PDMS composite material at 80℃ for 15 min. To consider the robustness of this hybrid nanogenerator, a separated conductive fabric was introduced as the counterpart electrode of triboelectric unit. Additionally, to improve the interaction between PDMS and graphite as well as PVDF and $BaTiO_3$, a small amount of MWCNTs was added into the corresponding composites[32].

Characterization: FTIR spectrum was conducted by FTIR spectrometer (Spectrum 100, PerkinElmer, US). A Raman spectroscopy (Spectra one Raman image system of Dilor with a CCD multi-channel detector) was utilized to investigate the structural changes of PDMS and PVDF composite films, wherein a 785-nm laser was used as the light source. Scanning electronic micrographs were taken by a scanning electron microscope (Hitachi TM3000). Surface roughness was obtained by a 3D optical surface profiler (Zygo, Nexview^{TM}).

Performance Measurement: The output performance of hybrid nanogenerator was evaluated by utilizing a Keyboard Life Tester (ZX-A03), which can provide a continuous dynamic sinusoidal motion with controlled levels of displacement from 0 to +10 mm and frequency from 1 to 5 Hz. The force signal was monitored by DAQ (Dewetron, Dewe-2600 DAQ system), and at the same time, the voltage signal was collected by Keisight DSO-X3014A oscilloscope and N2790A high voltage probe with 8 MΩ internal resistance. (The corresponding setup can be seen in Figure S3, Supporting information, and the corresponding internal circuit of Oscilloscope can be found in Figure S10, Supporting information.)

Supporting Information

Supporting Information is available from the Wiley Online Library or from the author.

Acknowledgements

The authors gratefully thank Dr. Jianliang Gong at The Hong Kong Polytechnic University for discussion, Scientific Officer Dr. Pang Siu Kwong at The Hong Kong Polytechnic University for help. The authors would like to acknowledge the funding supports from Research Grants Council of Hong Kong, Innovation and Technology Commission of Hong Kong SAR Government (Grant No.525113, 15215214, 15211016E, 15200917, ITP/039/16TP).

Received: January 12, 2018
Revised: February 14, 2018
Published online: April 14, 2018

References

[1] J. Chen, J. Yang, Z. Li, X. Fan, Y. Zi, Q. Jing, H. Guo, Z. Wen, K. C. Pradel, S. Niu, ACS nano 2015, 9, 3324.

[2] W. Zeng, X.-M. Tao, S. Chen, S. Shang, H. L. W. Chan, S. H. Choy, Energy & Environmental Science 2013, 6, 2631.

[3] W.-S. Jung, M.-G. Kang, H. G. Moon, S.-H. Baek, S.-J. Yoon, Z.-L. Wang, S.-W. Kim, C.-Y. Kang, Scientific reports 2015, 5.

[4] X. Pu, L. Li, M. Liu, C. Jiang, C. Du, Z. Zhao, W. Hu, Z. L. Wang, Advanced Materials 2016, 28, 98; Z. Tian, J. He, X. Chen, Z. Zhang, T. Wen, C. Zhai, J. Han, J. Mu, X. Hou, X. Chou, Nano Energy 2017; X. Ren, H. Fan, Y. Zhao, Z. Liu, ACS applied materials & interfaces 2016, 8, 26190; Z.-H. Lin, Y. Yang, J. M. Wu, Y. Liu, F. Zhang, Z. L. Wang, The journal of physical chemistry letters 2012, 3, 3599.

[5] S. Lee, W. Ko, Y. Oh, J. Lee, G. Baek, Y. Lee, J. Sohn, S. Cha, J. Kim, J. Park, Nano Energy 2015, 12, 410.

[6] H. Li, L. Su, S. Kuang, Y. Fan, Y. Wu, Z. L. Wang, G. Zhu, Nano Research 2017, 10, 785.

[7] F.-R. Fan, L. Lin, G. Zhu, W. Wu, R. Zhang, Z. L. Wang, Nano letters 2012, 12, 3109.

[8] S. Chen, X. Tao, W. Zeng, B. Yang, S. Shang, Advanced Energy Materials 2017, 7.

[9] S. H. Lee, Y. H. Ko, J. S. Yu, physica status solidi (a) 2015, 212, 401; T. Jiang, L. M. Zhang, X. Chen, C. B. Han, W. Tang, C. Zhang, L. Xu, Z. L. Wang, ACS nano 2015, 9, 12562; Y. Yao, T. Jiang, L. Zhang, X. Chen, Z. Gao, Z. L. Wang, ACS Applied Materials & Interfaces 2016, 8, 21398; V. Bhavanasi, V. Kumar, K. Parida, J. Wang, P. S. Lee, ACS applied materials & interfaces 2015, 8, 521.

[10] J. Gong, B. Xu, X. Tao, ACS applied materials & interfaces 2017, 9, 4988.

[11] X. Chen, S. Xu, N. Yao, Y. Shi, Nano letters 2010, 10, 2133; W. Wu, S. Bai, M. Yuan, Y. Qin, Z. L. Wang, T. Jing, ACS nano 2012, 6, 6231.

[12] Z. L. Wang, J. Song, Science 2006, 312, 242.

[13] M. Y. Choi, D. Choi, M. J. Jin, I. Kim, S. H. Kim, J. Y. Choi, S. Y. Lee, J. M. Kim, S. W. Kim, Advanced Materials 2009, 21, 2185.

[14] K.-I. Park, S. Xu, Y. Liu, G.-T. Hwang, S.-J. L. Kang, Z. L. Wang, K. J. Lee, Nano letters 2010, 10, 4939.

[15] H. Kim, T. Fernando, M. Li, Y. Lin, T.-L. B. Tseng, Journal of Composite Materials 2017, 0021998317704709.

[16] F. Fan, Z. Tian, Z. L. Wang, DOI.

[17] B. Yang, W. Zeng, Z. H. Peng, S. R. Liu, K. Chen, X. M. Tao, Advanced Energy Materials 2016, 6.

[18] V. L. Trinh, C. K. Chung, Small 2017.

[19] Z. L. Wang, ACS nano 2013, 7, 9533.

[20] C. Xue, J. Li, Q. Zhang, Z. Zhang, Z. Hai, L. Gao, R. Feng, J. Tang, J. Liu, W. Zhang, Nanomaterials 2014, 5, 36.

[21] I. S. Zaine, N. Napiah, A. Mohamad Yusof, A. Alias, A. Ali, S. H. Khalid, "Study on Dispersion and Characterization of Functionalized MWCNTs Prepared by Wet Oxidation", presented at *Applied Mechanics and Materials*, 2014.

[22] M. Pimenta, G. Dresselhaus, M. S. Dresselhaus, L. Cancado, A. Jorio, R. Saito, Physical chemistry chemical physics 2007, 9, 1276.

[23] M. Nour, K. Berean, S. Balendhran, J. Z. Ou, J. Du Plessis, C. McSweeney, M. Bhaskaran, S. Sriram, K. Kalantar-zadeh, international journal of hydrogen energy 2013, 38, 10494.

[24] E. A. d. Silva, D. Windmöller, G. G. Silva, K. C. d. S. Figueiredo, Materials Research 2017, 0.

[25] D. Maji, S. Lahiri, S. Das, Surface and Interface analysis 2012, 44, 62; D. Bodas, C. Khan-Malek, Microelectronic engineering 2006, 83, 1277.

[26] H. K. Park, S. M. Kim, J. S. Lee, J.-H. Park, Y.-K. Hong, C. H. Hong, K. K. Kim, Synthetic Metals 2015, 203, 127.

[27] M. Shahzad, M. Giorcelli, N. Shahzad, S. Guastella, M. Castellino, P. Jagdale, A. Tagliaferro, "Study of carbon nanotubes based polydimethylsiloxane composite films", presented at *Journal of Physics: Conference Series*, 2013.

[28] G. Zhu, C. Pan, W. Guo, C.-Y. Chen, Y. Zhou, R. Yu, Z. L. Wang, Nano letters 2012, 12, 4960.

[29] S. Niu, Y. Liu, S. Wang, L. Lin, Y. S. Zhou, Y. Hu, Z. L. Wang, Advanced Functional Materials 2014, 24, 3332.

[30] P. Bai, G. Zhu, Y. S. Zhou, S. Wang, J. Ma, G. Zhang, Z. L. Wang, Nano Research 2014, 7, 990.

[31] F. Saurenbach, D. Wollmann, B. Terris, A. Diaz, Langmuir 1992, 8, 1199; L.-H. Lee, Journal of electrostatics 1994, 32, 1.

[32] H.-C. Kuan, C.-C. M. Ma, W.-P. Chang, S.-M. Yuen, H.-H. Wu, T.-M. Lee, Composites Science and Technology 2005, 65, 1703.

Supporting Information

Highly flexible, large-scale and facile hybrid nanogenerator with cascaded piezoelectric and triboelectric units for mechanical energy harvesting

*Jian Song, Bao Yang, Wei Zeng, Zehua Peng, Shuping Liu, Jun Li, Xiaoming Tao**

1. Illustration of fabrication processes for PVDF and PDMS composite films

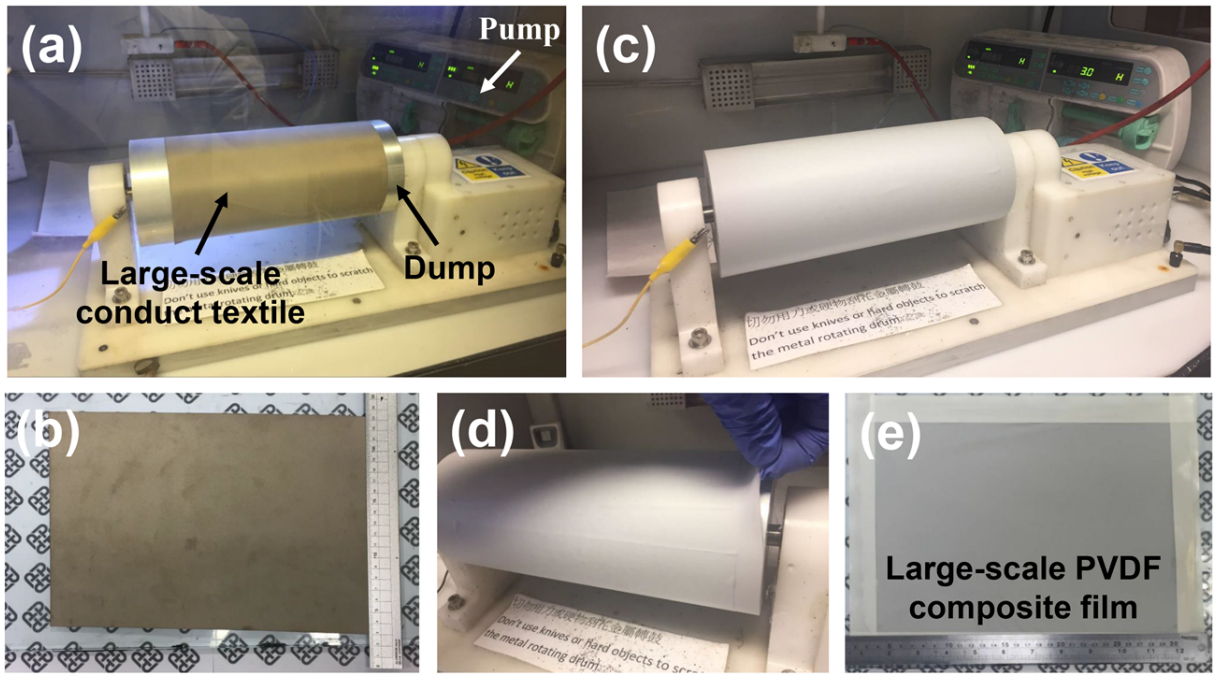

Figure S1. Fabrication process for PVDF composite film using electrospinning technique. (a) Electrospinning setup. (b) In the process of electrospinning. (d) Conductive textile fabric. (d-e) Illustration of as-fabricated PVDF composite film. Here, ahead of electrospinning, a conductive textile fabric with 28 cm×19 cm area was adhered on the rotating collector. After electrospinning, another textile fabric with same size was directly adhered on the other side of PVDF composite film. Thus, the piezoelectric unit (PEU) can be facile fabricated.

Actually, the nanofibers fabricated by electrospinning can be simultaneously polarized by the high voltage between needle and collector. Most of dipoles have been regularly

arranged as a specific direction along the nanofibers. Due to the existence of contact angle between the nanofiber and collector, the direction of nanofiber cannot be completely parallel. In the other word, the film can be polarized along the compressive direction, viz. d31 direction. In addition to the polarization process during the electrospinning, from the view of deformation, when a uniform external pressure is applied on the top surface of the piezoelectric unit, owing to the non-uniform deformation along the loading direction, the nanofibers can be partially rotated, from the in-plane direction (d_{31} mode) to the out-of-plane direction (d_{33} mode), and this possible reason has been discussed in our previous work.[1] In summary, the as-fabricated PVDF composite film do not need to be polarized any more.

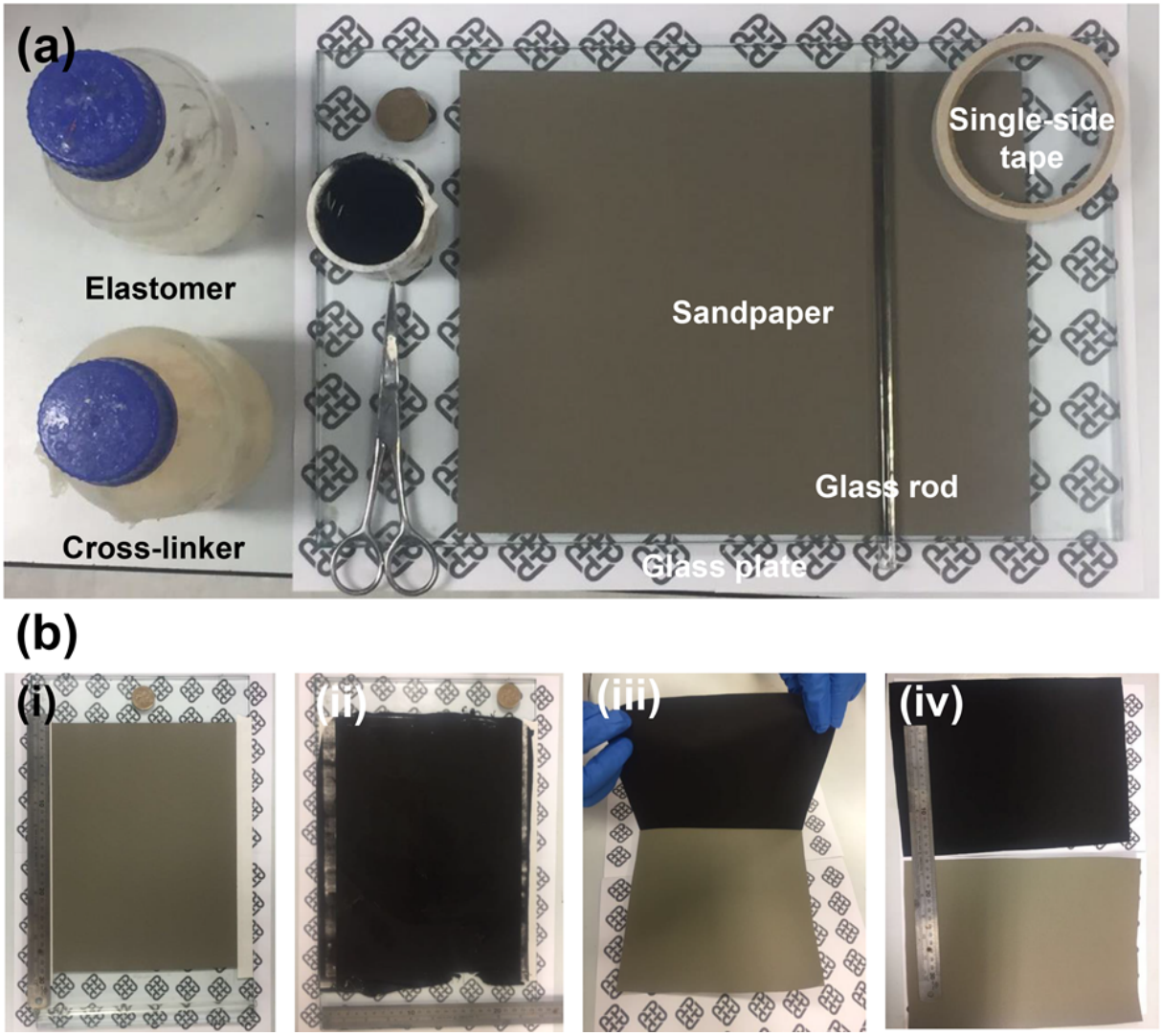

Figure S2. Fabrication process for PDMS composite film using doctor-blading method. (a) Materials and auxiliary equipment. (b) Illustration of fabrication process for PDMS composite film with a micro-pattern surface structure. Here, inexpensive sandpaper in term of the P3000 model was used to fabricate the PDMS composite film. Interesting, the as-prepared large-scale free-standing film can be perfectly peeled off from the sandpaper substrate without additional work.

2. Experimental setup

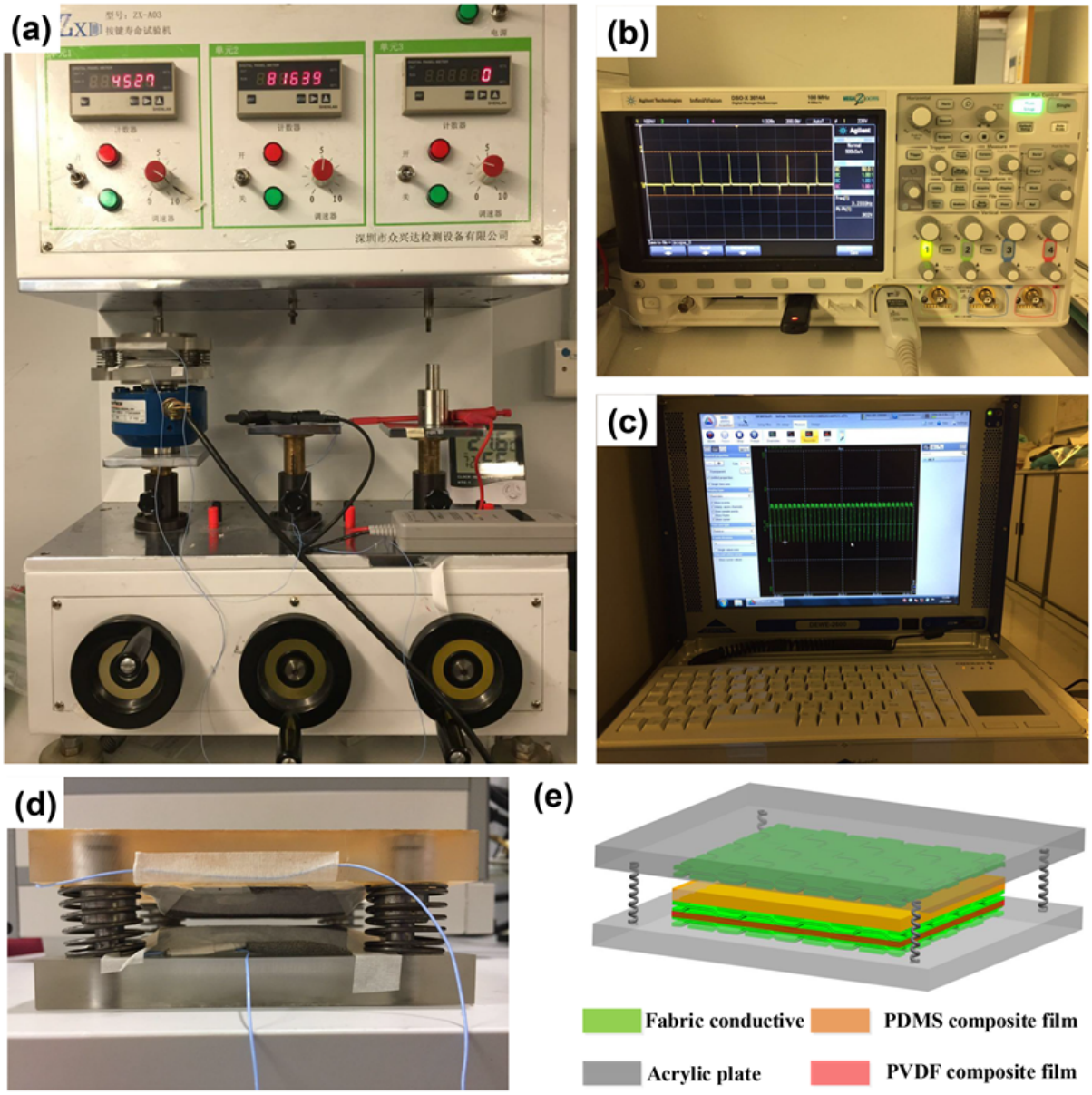

Figure S3. Experimental setup. (a) Keyboard life tester (ZXA-03). (b) Keisight DSO-X3014A oscilloscope and N2790A high voltage probe with 8 MΩ internal resistance. (c)

Load supervisor system (Dewetron, Dewe-2600 DAQ system). (d) A spring-assisted device to provide a cyclic compression excitation. (e) Schematic illustration of T-HNG assisted by a four-springs rigid device.

3. Internal SEM morphology, distribution and size of PVDF composite films

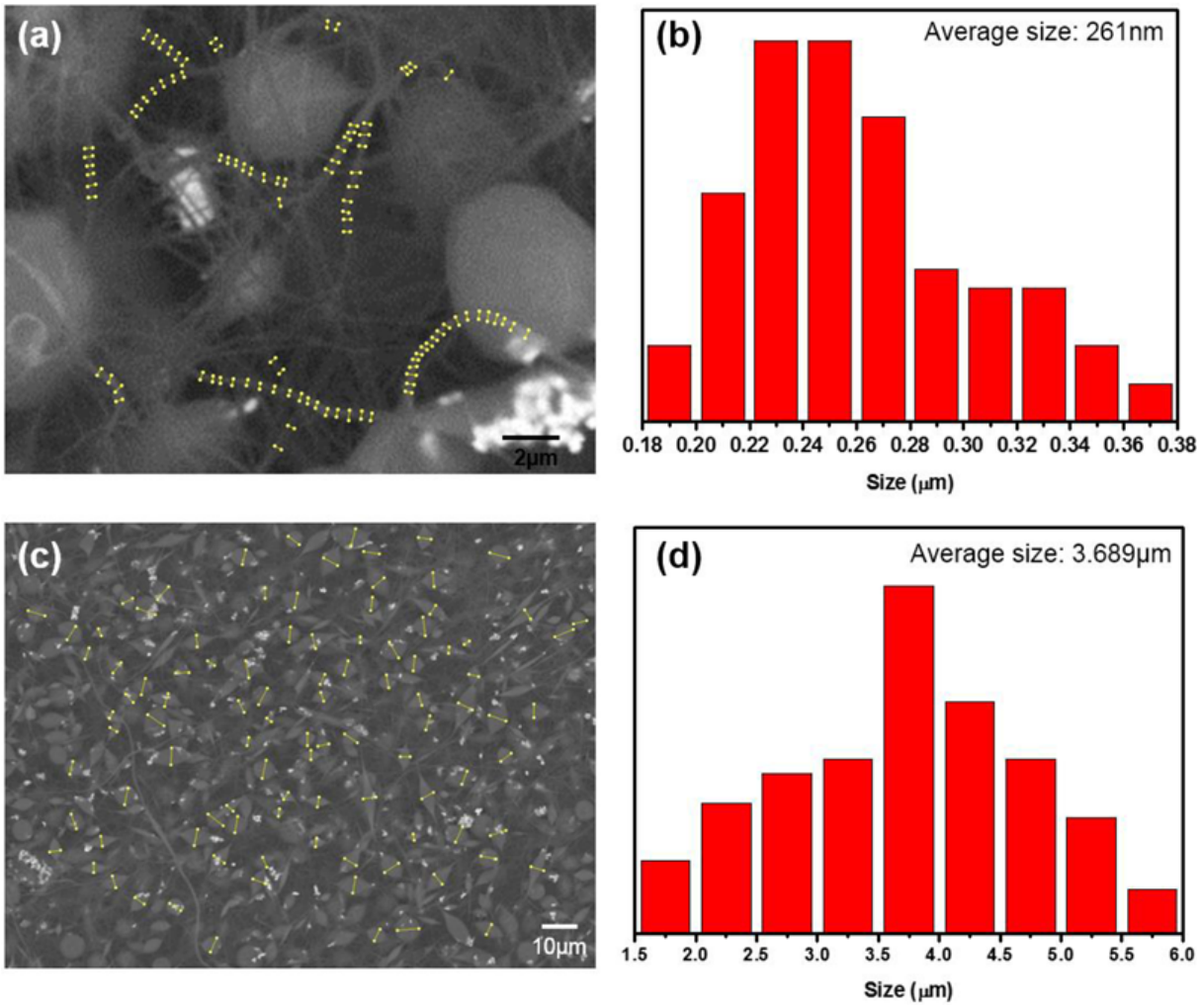

Figure S4. Internal SEM morphology, distribution and size of PVDF composite films. (a) SEM morphology of PVDF composite film. (b) Histogram of grain size for PVDF nanofibers. (c) Distribution of $BiTiO_3$. (d) Histogram of grain size for $BiTiO_3$ particles.

4. Raman spectra of additive materials

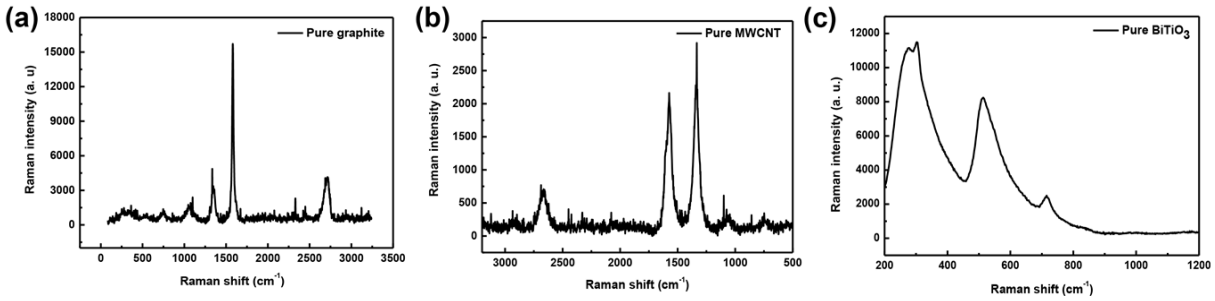

Figure S5. Raman spectra of additive materials. (a) Pure graphite. (b) Pure MWCNT. (c) Pure $BiTiO_3$.

5. Relative dielectric constant and electric conductivity of PDMS and PVDF films

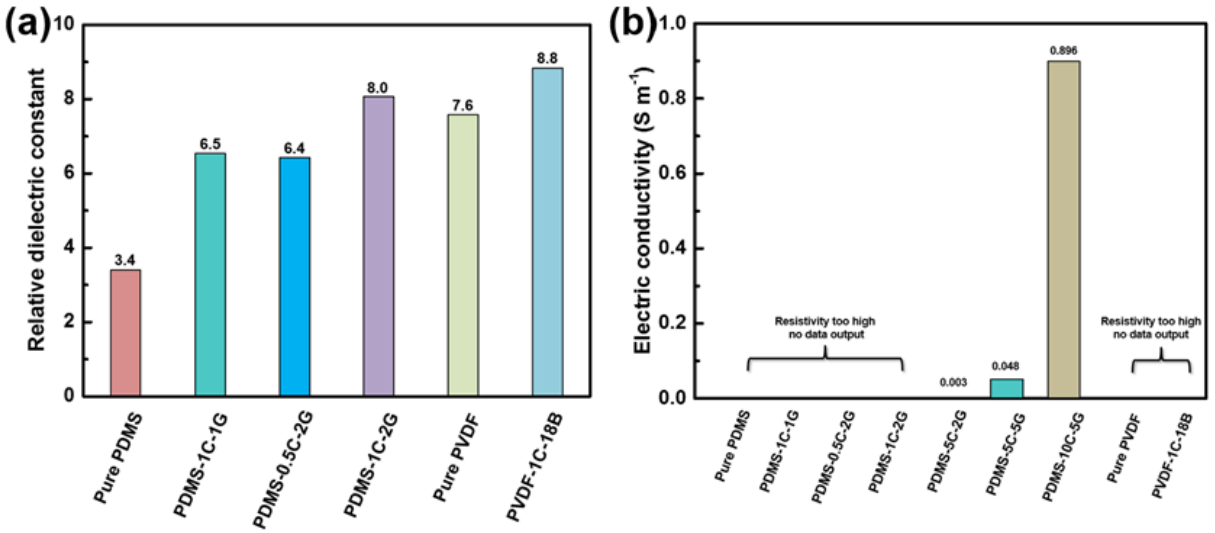

Figure S6. (a) Relative dielectric constant of various PDMS or PVDF composite films. (b) Electric conductivity of various PDMS or PVDF composite films. Here, the numbers represent the mass percentage of CNT or graphite. For the relative dielectric constant, the measure frequency is under 1000Hz.

6. Optimized triboelectric unit

To the best of our knowledge, surface roughness and conductive performance both have a remarkable influence on the output performance of nanogenerators.[2] It is therefore

necessary to investigate the influences of surface roughness and the contents of addictive components on the electric performances of TEU and PEU with rectification, separately.

Figure. S6(a) illustrates the output voltage vs. time curves based on TEUs with different surface roughness P0, P180, P600, P1000, P3000 and P5000, named P*-PDMS-TEUs (P* means the model of sandpaper in accordance with European Standard), respectively. To be the best of our knowledge, the electric performances are not only related to the peak voltage in the output voltage-time curves (Figure. S6(a)), but also can be influenced by the effective time interval. Thus, we used the effective surface charge density σ to estimate the electric performances of nanogenerators, which can be calculated by[3]

$$\sigma = \frac{Q}{2nS} = \frac{\int_0^{t_m} I\mathrm{d}t}{2nS} = \frac{\int_0^{t_m} U\mathrm{d}t}{2nSR_i} \quad \text{(S1)}$$

where Q is the amount of charges; U, I and R_i (8 MΩ) corresponds to the voltage, current and internal resistor (Oscilloscope probe); S is the area of contact surface; t_m is the measure time, which includes $2n$ half-cycle (n is the amount of cycles, $n = 16$). In accordance with Eqation (1), the charge densities induced by TEU for P180-PDMS-TEU, P600-PDMS-TEU, P1000-PDMS-TEU, P3000-PDMS-TEU and P5000-PDMS-TEU are 14.17 μC m^{-2}, 19.72 μC m^{-2}, 26.67 μC m^{-2}, 46.42 μC m^{-2} and 29.73 μC m^{-2}, respectively, whereas the P0-PDMS-TEU has only a tribo-charge density of 27.36 μC m^{-2}. Noteably, because the amount of transferred charges fully derived from the electrostatic induction and the max separation distance of TENGs is sufficiently large so that most of charges can transfer from one electrode to the other, we approximately adopted the method shown in Equation (S1) to evaluate the triboelectric or piezoelectric charge density.

It is noted that there are no clear regular between the performance enhancement of TEUs and the roughness. It can be ascribed to various surface morphologies (Figure. S6(c)) that changes the effective contact surface. The increase of the density of microhole improves the

roughness level, which to some degree enlarges the effective contact surface due to the elastic deformation of PDMS film and simultaneously makes the deformation of elastomer more easily. However, too many microholes can severely reduce the effective contact area of PDMS film, which finally results in decreasing the performance of TEUs. Therefore, for the P3000-PDMS-TEU, an enhanced electric performance approximately 1.6 times larger than that of P0-PDMS-TEU was achieved.

Figure. S6(b) investigates the effect of contents of additive components, viz. MWCNT and graphite, on the electric performances based on the P3000-PDMS-TEU. To be simplified, Our named three PDMS composite films with 1 wt% CNT/ 1 wt% graphite, 0.5 wt% CNT/ 2 wt% graphite and 1 wt% CNT/ 2 wt% graphite as PDMS-1C-1G-TEU, PDMS-0.5C-2G-TEU and PDMS-1C-2G-TEU, respectively. All the tribo-charges based on PDMS composite films are much higher than that based on the pure PDMS film, giving an indication of the improvement effect of MWCNT and graphite. Moreover, the PDMS-1C-2G-TEU has the highest charge density, viz. 49.44 $\mu C\ m^{-2}$, while the charge density is slightly higher than those of other two groups of TEUs (PDMS-1C-1G-TEU: 45.28 $\mu C\ m^{-2}$; PDMS-0.5C-2G-TEU: 48.75 $\mu C\ m^{-2}$).

To sum up, the optimized triboelectric unit is PDMS-1C-2G TEU, which has a roughness surface fabricated by using P3000 sandpaper.

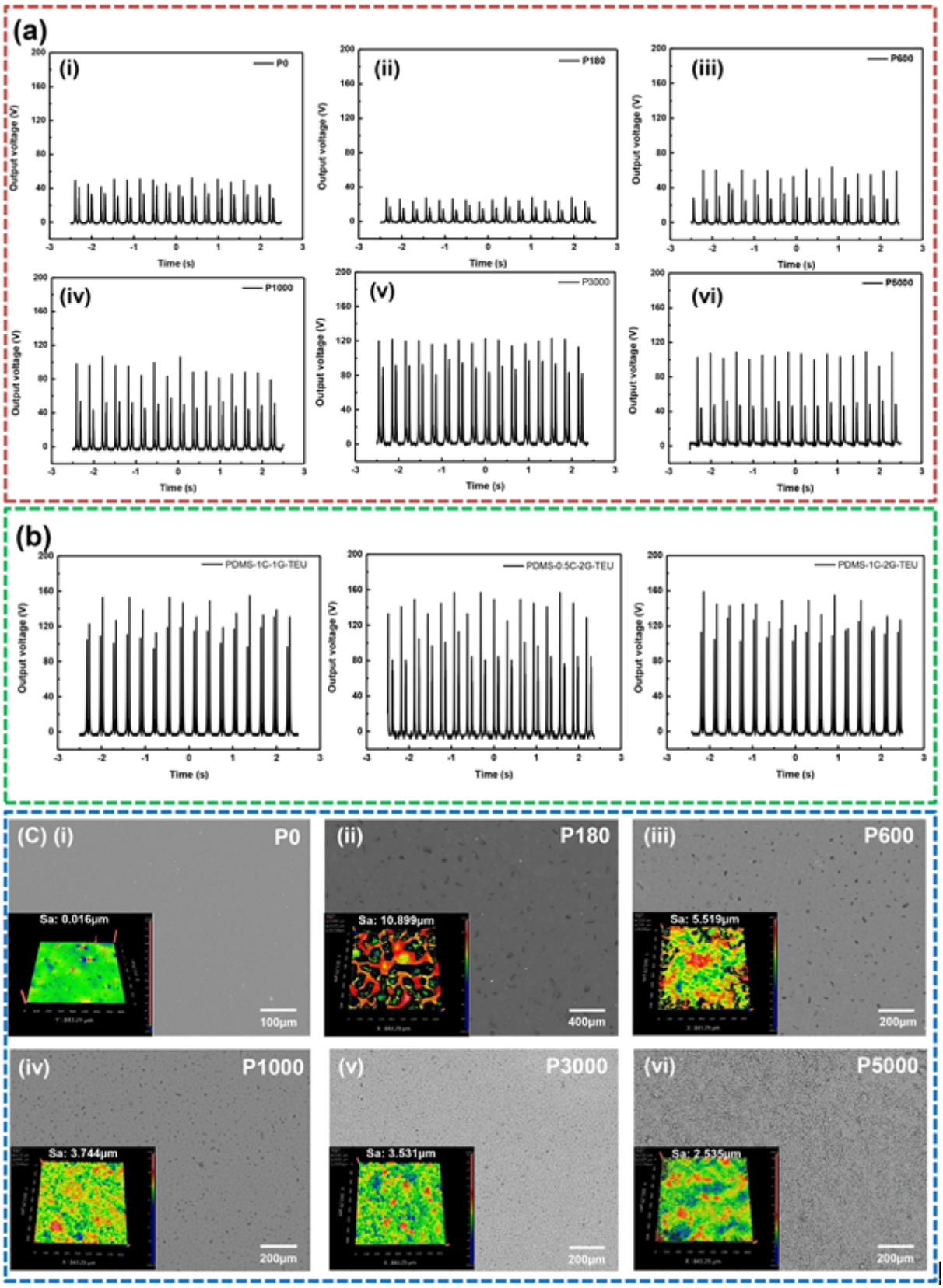

Figure S7. Optimized triboelectric unit and surface characteristic. (a) Comparison with TEUs with different surface roughness. (b) Comparison with TEUs with various contents of CNT

and Graphite. (c) SEM morphologies of TEUs with different surface roughness. Insets illustrate the corresponding surface roughness.

7. Optimized piezoelectric unit

Figure. S7 demonstrates the output voltage vs. time curves based on pure PVDF, 1 wt% CNT/ 6 wt% $BiTiO_3$ (PVDF-1C-6B), 1 wt% CNT/ 12 wt% $BiTiO_3$ (PVDF-1C-12B), 1 wt% CNT/ 18 wt% $BiTiO_3$ (PVDF-1C-18B), 1 wt% CNT/ 24 wt% $BiTiO_3$ (PVDF-1C-24B) and 0.5 wt% CNT/ 18 wt% $BiTiO_3$ (PVDF-0.5C-18B).

According to Eqation (S1), the charge densities induced by piezoelectric effect from 17.08 $\mu C\ m^{-2}$ to 48.19 $\mu C\ m^{-2}$ after adding MWCNT and $BiTiO_3$ particles, revealing that the electric performances of PEUs obviously depends on the contents of additive materials. Specifically, the maximum piezo-charge density of 48.19 $\mu C\ m^{-2}$ originates from the PEU with PVDF-1C-18B film, whereas the corresponding performance for PEUs with pure PVDF, PVDF-1C-6B, PVDF-1C-12B and PVDF-1C-24B films is 17.08 $\mu C\ m^{-2}$, 25.14 $\mu C\ m^{-2}$, 41.11 $\mu C\ m^{-2}$ and 20.00 $\mu C\ m^{-2}$, respectively, in the case of 1 wt% CNT. This result show that piezoelectric $BiTiO_3$ particles enclosed by PVDF nanofibers can significantly enhance the output performances of PEUs, especially in polymer-ceramic composites. This is due to that free charges accumulate by dipoles from PVDF and $BiTiO_3$, and therefore new dipoles are generated in the corresponding position that can improve the output performances of PEUs. Nevertheless, excessive amount of $BiTiO_3$ adversely affects the output performance, which can make the network of PVDF nanofibers more discontinuous and disorder.[4]

Additionally, the influence of the amount of MWCNT on the performance of PEUs has also been estimated, shown in Figure. S7. The result exhibits that the output voltage of PEUs is not sensitive to the content of CNT in the case of 18 wt% $BiTiO_3$ particles, which can be ascribed to the low content of MWCNT in this work.

In summary, the optimized piezoelectric unit is PVDF-1C-18B PEU.

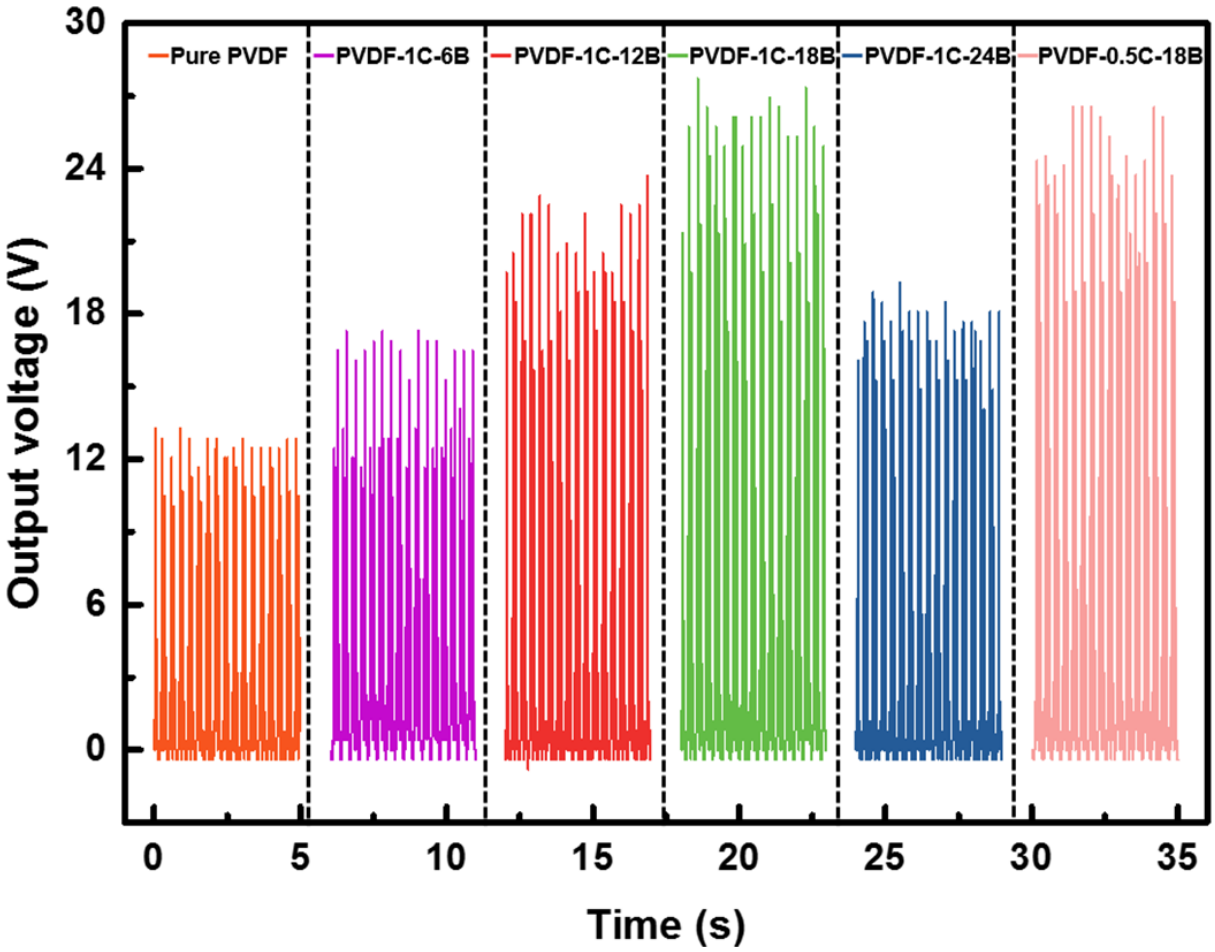

Figure S8. Comparison with piezoelectric units with different contents of $BiTiO_3$ and MWCNT.

8. Rectified output voltage vs. time curves based on PEU and TEU

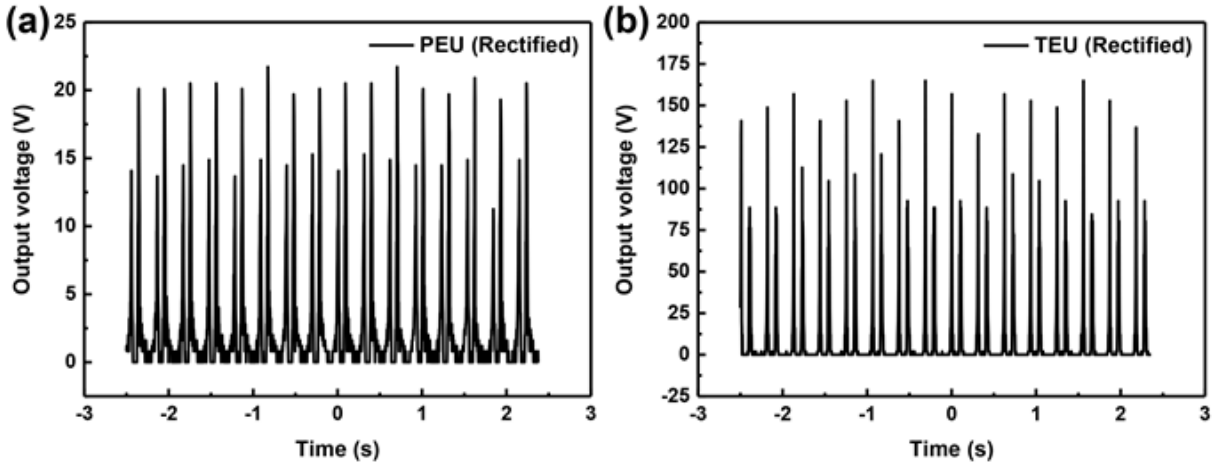

Figure S9. Rectified output voltage vs. time curves based on PEU (a) and TEU (b).

9. Schematic illustration of measurement circuit using Oscilloscope

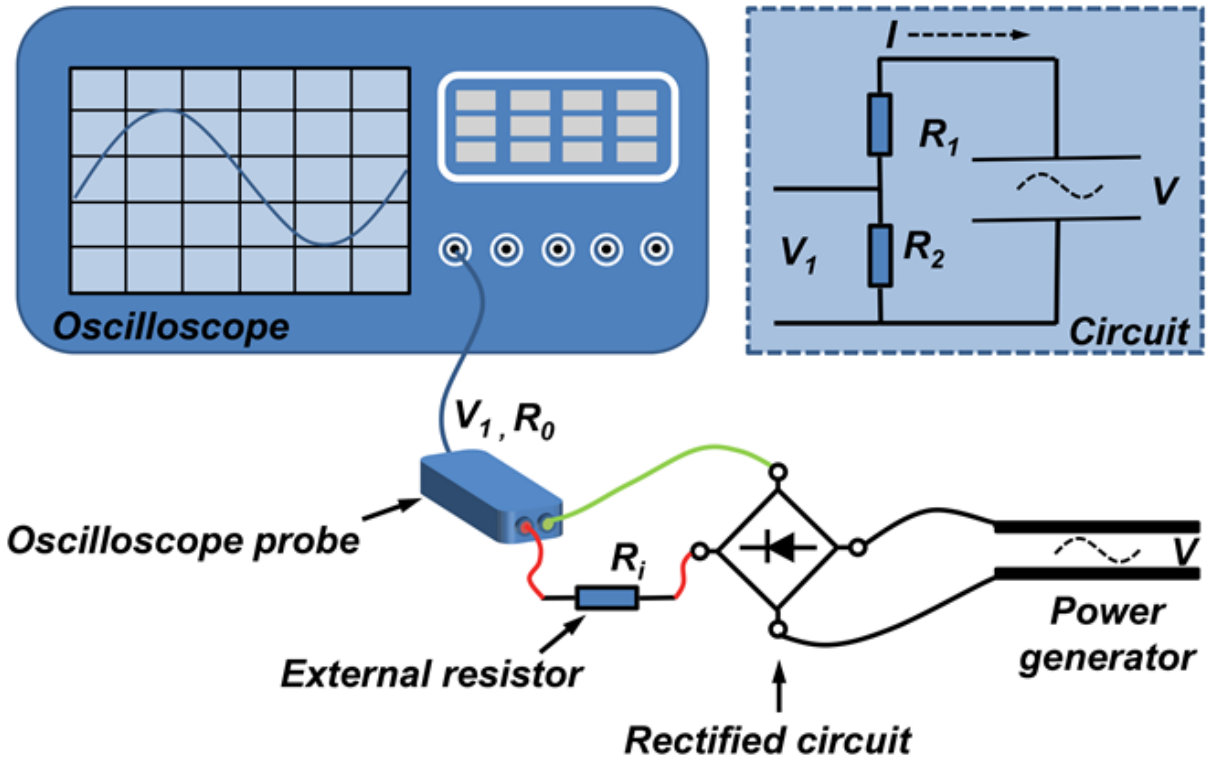

Figure S10. Schematic illustration of measurement circuit. Here, we can clearly see that the output alternating voltage is not entirely the case of open-circuit or short-circuit, which is due to the 8 MΩ (*Ro*) built-in resistor.

10. Theoretical derivation for conductor-to-dielectric triboelectric nanogenerator

After experiencing enough contact-separate cycles, the two triboelectric layers will have opposite static charges with equal density of σ, as a result of triboelectric effect.[5] Due to the electrostatic effect, when the electrode 1 (ED 1) is separated at a maximum distance of X_{max}, positive tribo-charges are completely screened on the ED 1, leaving an equal amount of induced positive charges on the electrode 2 (ED 2). We defined this case as the initial case of theoretical analysis, see Figure. S10.

In the case of *x*, according to the Gauss's law, we can obtain

$$E_a = -\frac{Q_1}{S\varepsilon_0} \tag{S2}$$

$$E_d = -\frac{Q_2}{S\varepsilon_0\varepsilon_r} \tag{S3}$$

where E_a and E_b are the electric field strength inside the air gap and dielectric layer, respectively; Q_1 and Q_2 are the amount of charges on EDs 1 and 2; ε_0 and ε_r are the vacuum permittivity and the relative permittivity.

Due to the close loop of electric potentials in circuit (Figure. S11), we can obtain

$$\sum_{i=1}^{N} V_i = 0 \tag{S4}$$

Substitute Eqation (S2) and (S3) into Eqation (S4), we can obtain

$$E_a x(t) + E_d d + V(t) = 0 \tag{S5}$$

where $x(t)$ and d are the air gap and thickness of dielectric; $V(t)$ is the voltage of nanogenerator at the time of t. In accordance with Ohm's law, $V(t)$ can be expressed as

$$V(t) = RI(t) = R\frac{\mathrm{d}Q}{\mathrm{d}t} \tag{S6}$$

where R is the external resistor; Q is the amount of transferred charges between EDs 1 and 2.

In the case of $t = 0$, the ED 1 is located at the maximum gap, and therefore the initial conditions can be obtained

$$\begin{cases} Q_1(t=0) = 0 \\ Q_2(t=0) = \sigma S = \dfrac{Q}{S} \end{cases} \tag{S7}$$

where σ is the surface charge density at a contact surface, induced by triboelectric effect. Merging Eqation (S5) and (S7), we can obtain

$$R\frac{\mathrm{d}Q}{\mathrm{d}t} + \left(d_r + x(t)\right)\frac{Q}{S\varepsilon_0} - \frac{\sigma}{\varepsilon_0}x(t) = 0 \tag{S8}$$

where d_r is the effective thickness constant ($d_r = d / \varepsilon_r$).

In conclusion, the *V*-*Q*-*x* relationship in contact-separation mode for conductor-to-dielectric category is built. Notice that during the process of theoretical derivation, the piezoelectric unit is in fact equivalent to the ED 2 owing to no work for that unit.

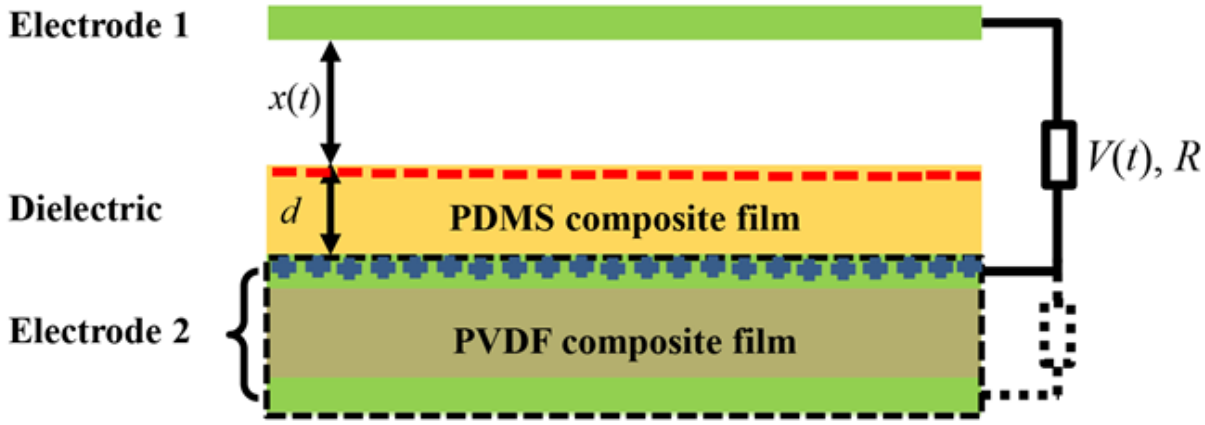

Figure S11. Schematic illustration of a conductor-to-dielectric triboelectric nanogenerator in contact-separation mode. Here, due to no work for PVDF composite film, the cascaded piezoelectric unit is considered as the electrode 2 during the process of theoretical analysis.

References

[1] W. Zeng, X.-M. Tao, S. Chen, S. Shang, H. L. W. Chan, S. H. Choy, Energy & Environmental Science 2013, 6, 2631.

[2] J. Gong, B. Xu, X. Tao, ACS applied materials & interfaces 2017, 9, 4988; S. Lee, W. Ko, Y. Oh, J. Lee, G. Baek, Y. Lee, J. Sohn, S. Cha, J. Kim, J. Park, Nano Energy 2015, 12, 410.

[3] Y. Zi, S. Niu, J. Wang, Z.Wen, W. Tang, Z. L. Wang, Nature Communications 2015, 6, 8376.

[4] U. Yaqoob, G.-S. Chung, Smart Materials and Structures 2017, 26.

[5] S. Niu, Y. Liu, S. Wang, L. Lin, Y. S. Zhou, Y. Hu, Z. L. Wang, Advanced Functional Materials 2014, 24, 3332.